UNIVERSITÀ DEGLI STUDI DI PAVIA
Facoltà di Ingegneria
Dipartimento di Ingegneria Civile e Architettura

Assessment of patient-specific aortic hemodynamics using Computational Fluid Dynamics (CFD)

Valutazione patient-specific dell'emodinamica dell'aorta attraverso analisi computazionali fluidodinamiche (CFD)

Supervisor:
Prof. Ferdinando Auricchio

Co - supervisors:
Ing. Adrien Lefieux
Dr. Simone Morganti

Author:
Silvia Cabiddu
UIN **404510**

Academic year 2012/2013

Sono le scelte che facciamo, Harry,
che dimostrano quel che siamo veramente,
molto più delle nostre capacità.
-Albus Silente-

Abstract

The purpose of this thesis is to evaluate patient-specific hemodynamic of a healthy aorta through computational fluid dynamic analysis (CFD) . To achieve it, we combined the CFD techniques with imaging techniques; this allows us to approximate the blood flow real behavior.

The aortic arch has a complex structure, with bifurcations, non-planar curvature, varying cross-sections. Understanding the effects of the curvature on the flow is an important task, to measure and interpret human hemodynamics in the aortic arch like flow axial velocity, vorticity and wal shear stress. For this reason, we initially studied the effects of curvature on the flow, creating a simplified model of the aorta(called candy cane), with a 180° planar bend.

In the first part of the thesis we show the effects of the curvature on the simple model using a steady inflow. Since in real cases the blood flow is not steady, we study the effects of a pulsatile flow in a candy cane. Comparing the results of the candy cane with two different inflow, we found opposite behavior of the velocity.

In the last part, we moved on a real case, which requires pulsatile inflow. The results show a similar behavior between the candy cane and the aorta, with the same pulsatile inflow. It means that the candy cane, with unsteady inflow, can be used as a suitable first model of an aorta for which many theoretical results exits. As a consequence, we showed that the pulsatility of the flow is a fundamental parameter to take into account for the study of the blood flow in the aorta.

Sommario

Lo scopo di questa tesi è la valutazione patient-specific dell'emodinamica di un aorta sana attraverso analisi computazionali fluidodinamiche (CFD). Per poter simulare l'evoluzione del flusso del sangue in una geometria patient-specific, approssimandone opportunamente in suo comportamento reale, si affiancheranno le tecniche di analisi CFD con le tecniche di imaging.

L'arco aortico umano presenta una struttura complessa, con biforcazioni, curvature non planari, variazione del diametro. Per misurare e interpretare l'emodinamica nell'arco aortico umano è importante capire gli effetti della curvatura sul flusso. Per questo motivo ci si è concentrati su questo aspetto.

Nella prima parte della tesi si discuteranno gli effetti della curvatura su un modello semplificato dell'aorta, chiamato candy cane, costituito da una curvatura planare di 180°, a cui è stato applicato in ingresso un flusso costante.

Poichè nei casi reali il flusso sanguigno non è mai costante si è deciso di studiare l'effetto della pulsatilità, applicando in ingresso a un candy cane un flusso pulsatile.

I risultati per i due casi mostrano un comportamento opposto del flusso.

Nell'ultima parte si è passati a studiare il caso reale, in cui si è applicato in ingresso un flusso pulsatile, lo stesso utilizzato nel caso del candy cane. I risultati trovati per l'aorta e per il candy cane con flusso pulsatile in ingresso, mostrano un comportamento molto simile del flusso nei due casi, mettendo in luce che il candy cane rappresenta una buona idealizzazione dell'aorta, per il quale esistono molti risultati teorici. Un altro risultato molto importante tener conto quando si studia il flusso di un aorta è la pulsatilità del flusso.

Contents

List of Tables

List of Figures

Chapter 1

Introduction

Describe the blood flow in the cardiovascular system is a hard task. The blood flow, through cardiovascular system, is the main responsible of the nutrient transport, oxygen and other molecules to and from the various organs. Because of this it is necessary to have a mathematical model to describe blood flow.

Already in 1775 Leonhard Euler studied to develop a system of equations with the goal to describe the blood flow in the arteries; however this equations are available for inviscid flow i.e, flow of an ideal fluid that does not have viscosity. The flow of a “real” viscous fluid (like blood) is described by the Navies Stokes equations. The Navier-Stokes equations were written almost one hundred eighty years ago. In fact, they were proposed in 1822 by the French engineer Claude-Louis Navier on the base of a suitable molecular model. However, the laws of interaction between the molecules postulated by Navier were not suitable for several materials and, in particular, for liquids. It was only more than twenty years later that the same equations were rederived by George Gabriel Stokes (1845) in a quite general way, by the assumption that the fluid, is continuum, in other words is not made up of discrete particles.

The fluid of interest to us is the blood. Blood is composed of corpuscular part, blood cells (leukocytes, thrombocytes and erythrocytes) suspended in liquid part, so blood is not a continuum fluid. Thus the continuum hypothesis for blood is not available in the smallest capillaries, since here the size of a red blood cell becomes comparable to that of the vessel, so we can not neglect the discrete nature of the blood. Due to this we shall focus our investigation on flow in large and medium sized vessels,where the size of red blood cells is much smaller than that of vessels and therefore the discrete nature of the blood can be neglected and we can consider it as continuum.

In this assay will describe the flow of blood by the Navier Stokes equations. These equations are nonlinear partial differential equations, hard to solve analytically,except in special cases. Thus most of the time only the numerical solution is available .

The numerical solution is computable by the methodology of **CFD(Computational Fluid Dynamics)** (computational fluid dynamics). The basic principle of the CFD is the transformation of differential equations, that describe the behavior of the fluid, in approximate equations, which are solved discretizing the time and the three-dimensional geometries by appropriate techniques such as finite element method. Because the equations are solved in finite number of points, the numerical simulation introduces an error (for the calculation of the error see Section 3.3).

The operational phases of a CFD simulation are summarized in Figure 1.1

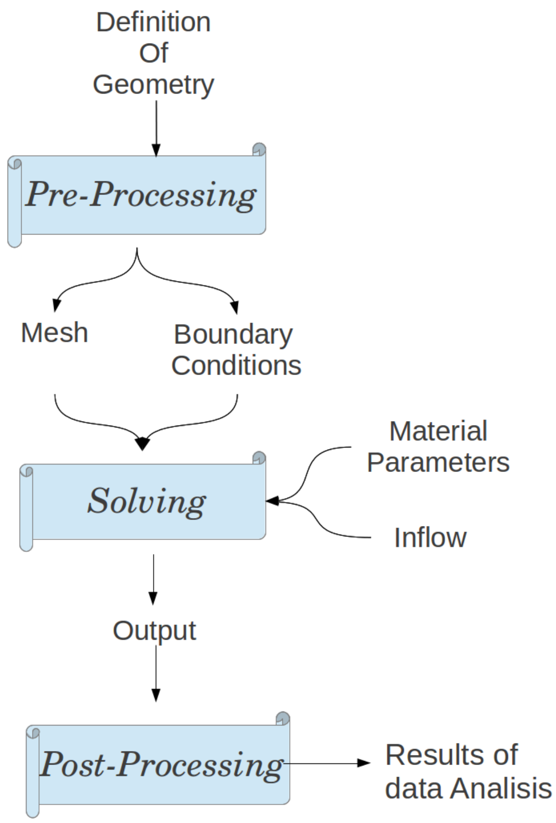

Figure 1.1: CFD Steps

Numerical models require data from patients particularly the value of the parameters characterizing the properties of blood and possibly: the vessel walls, the initial and boundary conditions to the resolution of the partial differential equations, as well as geometrical data that defines the shape of the computational domain. The latter can be obtained by imaging techniques (MRI) such as magnetic resonance imaging or computer tomography to (TC).

The use of CFD, with imaging techniques, to study blood flows have a lot of benefits. Firstly numerical simulations are of course less invasive than those in vivo, and potentially more accurate and flexible than those in vitro. Secondly, it allows to do a simulation patient specific, so it can help the surgeon in understanding how different surgical solutions may affect blood circulation and may guide the choice for the most appropriate procedure. Finally,low cost is another advantage.

The purpose of this thesis is the patient-specific study of hemodynamics of Aorta, simulate by **LifeV** a finite element library. Before it, we will start studying the blood flow through simplest models of the vessel geometry, a tube, then move on to more realistic geometries.

The thesis is organized as follows:

- In the second chapter we introduce the mathematical model, assuming that the blood may be regarded as a viscous fluid, incompressible and with constant density. Also we show a case for which the Navier-Stokes equations admits analytical solution: the Poiseuille flow.

- In the third chapter we talk about the procedure used for the simulations. In addition, for the Poiseuille flow (one of the few cases for which the Navier Stokes equations admit solution), we demonstrate that the numerical results good approximate the analytical ones, introducing an error which, as we will demostrate, depends on the fineness of the mesh.

- In the fourth chapter, we analyze the blood flow in a curved pipe, to highlight the effects that the curvature has on the flow. Understand this effects is important to measure and interpret the flow dynamics in the complex geometry of the human aortic arch.

- In chapter 5 we study the hemodynamics of a patient-specific aorta through the CFD method. In the first part of this chapter we explain how we derived the computational domain. Then we show the numerical results. The studies described in the chapter four, on the flow development in curved tubes provide excellent insight on the nature of the secondary flow and the resulting skewing of the axial velocity profiles. But in the human aorta, the flow development is further complicated by the non circular cross-sectional geometry, secondary and tertiary curvatures, tapering, etc.

Chapter 2

Mathematical Model

In vertebrates, blood is composed of corpuscular part (blood cells) suspended in liquid part. The liquid part is called plasma and is composed: 90% by water and 10% byorganic substances. The most important blood cells are: leukocytes, thrombocytes and erythrocytes, the last are the most numerous so they influence the behavior of blood greater than the other. The red blood cells are the main responsible for the special mechanical propriety, in particular the behavior of this cells may explain the principal features of blood like shear-thinning. Shear-thinning means that the fluid viscosity decreases with the increase of the rate of deformation. This effect is stronger in smaller vessels. Also below a critical vessel calibre (about 1 mm), blood viscosity becomes dependent on the vessel radius and decreases. Instead, increase of speed deformation produces a decrease of viscosity because into the vessel the red blood cells move to the central part of the capillary, whereas the plasma stays in contact with the vessel wall. This layer of plasma facilitates the movement of the red cells, thus causing a decrease of the viscosity [8].

We can separate models for blood flow in:

- Newtonian model, which neglects shear thinning so is suitable in larger vessels;
- Non-Newtonian.

As discussed above, when the diameter of the vessel is less that 1mm, the assumption that blood is a Newtonian fluid is hard to apply.

In our treatment we consider the aorta (d=3.3 cm), which takes part among the medium an large blood vessels (d>0.1cm). For this category of vessels we assume that the blood is:

Continuum Fluid is said continuum if it neglects its atomic or molecular structure, so that we can consider it continuous. The blood fluid is not continuous, but a suspension of cells. Since the aorta has much larger dimensions than those of the red blood cell, that have a dimension of the order of μm, we can neglect the particles present in the blood.

Homogeneous It means that $\rho(x,t) = 0, \quad \forall x \in D, \quad \forall t$ where x represents a portion of the fluid.

Incompressible Fluid is incompressible if is not reduced in volume on increase in pressure. This assumption is valid because the compressibility of liquids, and then the blood, is generally very low, and negligible for fluid dynamic problems.

Newtonian Fluid is Newtonian if the relation between the shear stress tensor and the rate of strain is linear. The proportionality constant is called viscosity.

This assumptions allow us to simplify the Navier-Stokes equations, which are described in the next section. Also will not be introduced any turbulence model, because the blood flow is laminar, i.e the layers of fluid slide one above the other, without mixing, unlike of the turbulent flow, where they are randomly mixed .

In the next section we derive the Navier-Stokes equations for a continuum, incompressible and Newtonian fluid.

2.1 Navier-Stokes Equations

The general Navier–Stokes equations derived from the basic principles of conservation of:

- Mass;
- Momentum (linear and angular momentum);
- First principle of thermodynamics;
- Second principle of thermodynamics.

In our treatment, we assume that the flow is isothermic, it means that the flow remains at the same temperature while flowing in a conduit. Under this constraint the mass and momentum conservation law are independent from the energy conservation one, so **the Navier Stokes equation is derived from mass and momentum conservation**.

The conservation equations describe the variation in time and the spatial distribution of the physical quantities of interest. These equations are applied in a region of space of arbitrary shape **call control volume** Ω. The most general form of the equations of conservation say that: *"the changes of some extensive property (mass, momentum, energy, etc) defined over a control volume Ω must be equal to what is lost (or gained) through the boundaries of the volume plus what is created/consumed by sources and sinks inside the control volume"*.

2.1.1 Mass Conservation

The principle mass conservation can be expressed as [18]:

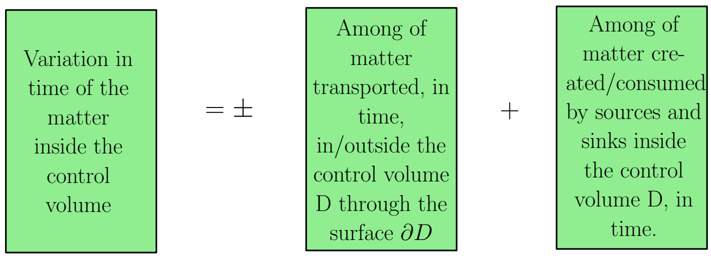

Figure 2.1: Conservation law

Suppose we have a body Ω and consider a control volume $D \subset \Omega$ like in Figure 2.2.

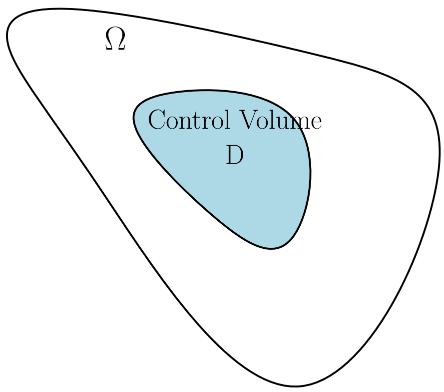

Figure 2.2: Control volume $D \subset \Omega$

The amount of matter contained in D is:

$$\int_D \rho(x,t)\, d\Omega \quad \text{with} \quad x \in \Omega \quad \text{and} \quad t \geq 0 \tag{2.1}$$

where ρ $[g/cm_3]$ is the density and is a function of space and time. The instantaneous change of the among of matter inside the control volume can be written as:

$$\frac{d}{dt}\int_d \rho(x,t)\, d\Omega \tag{2.2}$$

Assuming that in our system there are not sources and sinks, the second term to the right-hand, in the equation represents by the Figure 2.1, is zero. Under this hypothesis, in the case of motion of a fluid, we can express the conservation of mass in terms of Lagrangian point of view, which says that: *"The mass contained in a volume, that moves with the fluid does not* *change in time"*. Thus, the Equation 2.2 can be rewritten as:

$$\frac{d}{dt}\int_D \rho(x,t)\, d\Omega = F_{Total} \tag{2.3}$$

where we denote by F_{Total} the amount of total mass transports in time through the surface ∂D of the control volume. This term is given from the difference between the incoming and outgoing flow through the surface.

$$F_{Total} = Flux_{in} - Flux_{out} \tag{2.4}$$

To assess if a flow is incoming or outgoing through the surface, we consider the oriented surface ∂D (see Figure 2.3), for each surface element ds, we can associate the normal vector $\vec{n}$, which can be considered incoming or outgoing to the surface. By convention we consider positive the outward normal from the surface element.

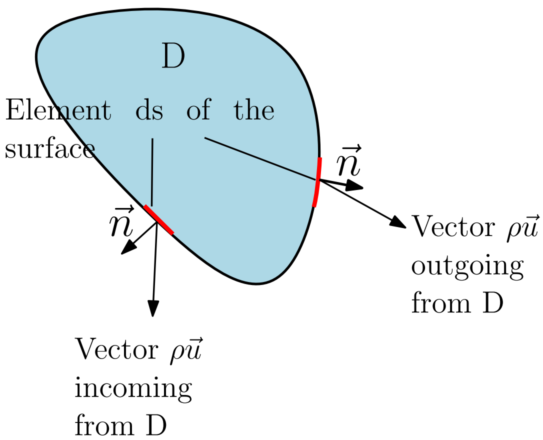

Figure 2.3: Flow through the control volume D

The total flow of material through the surface can be expressed as:

$$F_{Total} = -\int_{\partial D} \rho(\vec{u}\cdot\vec{n})\, ds \tag{2.5}$$

substituting the Equation 2.5 in the Equation 2.3 and swapping the order of differentiation in the first term, it follows that:

$$\int_D \frac{\partial\rho(x,t)}{\partial t}\, d\Omega = -\int_{\partial D} \rho(\vec{u}\cdot\vec{n})\, ds \tag{2.6}$$

we rewrite the Equation 2.6 using the divergence theorem to express the total flux through the surface ∂D in terms of integral volume rather than surface integral:

$$\int_D \frac{\partial \rho(\Omega, t)}{\partial t}\, d\Omega = -\int_D \nabla(\rho(\vec{u}))\, d\Omega \quad \forall t \tag{2.7}$$

bringing all the terms on the same side of the equal sign and transform the sum of volume integrals in the volume integral of the sum of the integral functions, we obtained:

$$\int_D [\frac{\partial \rho(\Omega, t)}{dt} + \nabla(\rho(\vec{u}))] = 0 \tag{2.8}$$

thus the Equation 2.8 must be valid for all D, we can write:

$$\frac{\partial \rho(\Omega, t)}{dt} + \nabla(\rho(\vec{u})) = 0 \quad \forall t \quad \forall D \tag{2.9}$$

The Equation 2.9 is called continuity equation and if we assume that ρ is constant, the law of conservation of mass becomes:

$$\nabla \cdot \vec{u} = 0 \tag{2.10}$$

2.1.2 Conservation Of Momentum

Suppose we have a body Ω and consider a volume $D \subset \Omega$ (the same as used in Section 2.1.1) Figure 2.2.

The equation of conservation of momentum is obtained by the second principle of dynamics; it says that: *"The variation of momentum is equal to the resultant of the forces acting on D"*.

Also in this case the principle of conservation of momentum can be expressed as [18]:

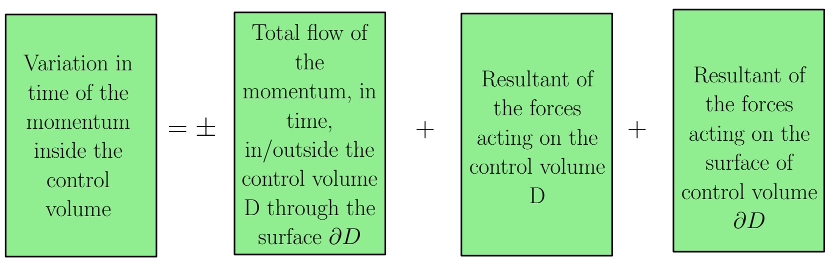

Figure 2.4: Conservation of momentum

The amount of momentum associated with a volume $D \subset \Omega$ is:

$$\int_D \rho(x, t)\vec{u}\, d\Omega \tag{2.11}$$

while the instantaneous change of the among of momentum inside the control volume is:

$$\frac{d}{dt}\int_D \rho(x,t)\vec{u}\,d\Omega \tag{2.12}$$

Before proceeding with the derivation of the conservation of momentum, we introduce the **material derivative**. The material derivative [18] describes the time rate of change of some physical quantity (like momentum) for a material element subjected to a space-and-time-dependent velocity field.

The material derivative can serve as a link between Eulerian and Lagrangian descriptions. In fact changes in properties of a moving fluid can be measured in two different ways. One can measure a given property by either carrying out the measurement on a fixed point in space as particles of the fluid pass by, or by following a parcel of fluid along its streamline. The derivative of a field with respect to a fixed position in space is called the Eulerian derivative while the derivative following a moving parcel is called the material derivative.

The material derivative is defined as the operator:

$$\frac{D}{Dt} \stackrel{def}{=} \frac{\partial}{\partial t} + \vec{u}\cdot\nabla \tag{2.13}$$

where $\vec{u}$ is the velocity of the fluid. The first term on the right-hand side of the equation is the ordinary Eulerian derivative (i.e. the derivative on a fixed reference frame, representing changes at a point with respect to time) whereas the second term represents changes of a quantity with respect to position. Applying the material derivative at the among of momentum, we find:

$$\frac{D}{dt}\int_D \rho\vec{u}\,d\Omega = \frac{\partial}{\partial t}\int_D \rho\vec{u}\,d\Omega + \vec{u}\cdot\nabla\rho\vec{u}\,d\Omega \tag{2.14}$$

swapping the order of differentiation, and transform the sum of integrals in the volume integral of integral functions, the terms on right-hand side of the equations became:

$$\int_D \rho[\frac{\partial\vec{u}}{\partial t} + \vec{u}\cdot\nabla\vec{u}]\,d\Omega \tag{2.15}$$

The Equation 2.15, represents the first two terms of the equation in Figure 2.4.

Now we have to defined the resultant of forces acting in our system. In particular, the forces can be divided into two categories: the surface forces acting on the surface control volume and the volume forces acting on the control volume itself.

The surface forces that act on each small volume of real viscous fluid are: pressure forces (normal stresses) and tangential stresses (also called shear tresses); while body force for example are gravity.

The pressure giving rise to force on the surface ∂D, which we express as:

$$\int_{\partial D} -p\vec{I}\vec{n}dS \tag{2.16}$$

Where $\vec{I}$ is the 3x3 identity matrix.

Applying the divergence theorem to switch from a surface integral to a volume integral at the Equation 2.16, we rewrite it as:

$$\int_{D} -\nabla \cdot p\, d\Omega \tag{2.17}$$

The shear stress, in general, can act in any direction at the different points on ∂D so that is represented by full tensor

$$\begin{bmatrix} T_{xx} & T_{xy} & T_{xz} \\ T_{yx} & T_{yy} & T_{yz} \\ T_{zx} & T_{zy} & T_{zz} \end{bmatrix} \tag{2.18}$$

and the force due to the shear stresses is given by:

$$\int_{\partial D} \vec{T}\vec{n}\, dS \tag{2.19}$$

Also in this case we apply the divergence theorem:

$$\int_{D} \nabla \cdot \vec{T}\, d\Omega \tag{2.20}$$

Substituting the terms that we found in the Equations:2.15,2.17,2.20 in the law of conservation of momentum represent in Figure 2.4, we obtained

$$\int_{D} \rho[\frac{\partial \vec{u}}{\partial t} + \vec{u} \cdot \nabla\vec{u}]\, d\Omega = \int_{D} -\nabla \cdot p d\Omega + \int_{D} +\nabla \cdot \vec{T}\, d\Omega \tag{2.21}$$

bringing all the terms on the same side of the equal sign and transform the sum of volume integrals in the volume integral of the sum of the integral functions, we obtained:

$$\int_{D} \rho[\frac{\partial \vec{u}}{\partial t} + \vec{u} \cdot \nabla\vec{u}] + \nabla \cdot p - \nabla \cdot \vec{T}\, d\Omega = 0 \tag{2.22}$$

We assumed that the blood is Newtonian, it means that the shear stress tensor is a linear function of the rate of strain tensor, in mathematical terms this is expressed as:

$$\begin{aligned} T &= \mu\vec{\epsilon} + \lambda Trace(\vec{\epsilon})\vec{I} \\ \text{with} \quad \vec{\epsilon} &= \frac{1}{2}[\nabla\vec{u} + \nabla\vec{u}^T] \end{aligned} \tag{2.23}$$

Where $\vec{\mu}$ and $\vec{\lambda}$ are parameters describing the "stickiness" of the fluid. For an incompressible fluid $\vec{\lambda}$ is not important because $Trace(\vec{\epsilon}) = \nabla \cdot \vec{u} = 0$, in fact we have

$$\nabla \cdot \vec{u} = \begin{bmatrix} \partial u_x/\partial x & \partial u_x/\partial y & \partial u_x/\partial z \\ \partial u_y/\partial x & \partial u_y/\partial y & \partial u_y/\partial z \\ \partial u_z/\partial x & \partial u_z/\partial y & \partial u_z/\partial z \end{bmatrix} \tag{2.24}$$

while $\vec{\epsilon}$ in matricial form is:

$$\vec{\epsilon} = \frac{1}{2}[\begin{bmatrix} \partial u_x/\partial x & \partial u_x/\partial y & \partial u_x/\partial z \\ \partial u_y/\partial x & \partial u_y/\partial y & \partial u_y/\partial z \\ \partial u_z/\partial x & \partial u_z/\partial y & \partial u_z/\partial z \end{bmatrix} + \begin{bmatrix} \partial u_x/\partial x & \partial u_y/\partial x & \partial u_z/\partial x \\ \partial u_x/\partial y & \partial u_y/\partial y & \partial u_z/\partial y \\ \partial u_x/\partial z & \partial u_y/\partial z & \partial u_z/\partial z \end{bmatrix}] \tag{2.25}$$

it follows that

$$Trace(\vec{\epsilon}) = \frac{\partial u_x}{\partial x} + \frac{\partial u_y}{\partial y} + \frac{\partial u_z}{\partial z} = \nabla \cdot \vec{u} = 0 \tag{2.26}$$

so for a three-dimensional flow $2\lambda + 3\mu \geq 0$; μ measuring the resistance of the fluid to shearing, give arise to the viscous shear force.

Now we can prove that:

$$\nabla \cdot T = \mu \nabla \cdot \vec{u} \quad \text{so} \quad \mu \nabla \cdot \vec{\epsilon} = \mu \nabla^2 \cdot \vec{u} \tag{2.27}$$

Replacing the Equation 2.27 in 2.22, we get:

$$\int_D \rho[\frac{\partial \vec{u}}{\partial t} + \vec{u} \cdot \nabla \vec{u}] + \nabla \cdot p - \nabla \cdot (\mu \nabla \cdot \vec{u})\, d\Omega = 0 \tag{2.28}$$

thus the Equation 2.28 must be valid for all D, we can write:

$$\rho[\frac{\partial \vec{u}}{\partial t} + (\vec{u} \cdot \nabla \vec{u})] + \nabla p - \mu \nabla^2 \vec{u} - \vec{f} = 0 \quad \text{on } D \subset \Omega \tag{2.29}$$

Because the density is constant, we divide all term of the Equation 2.29 by ρ and we find:

$$\frac{\partial \vec{u}}{\partial t} + (\vec{u} \cdot \nabla \vec{u}) = -\frac{\nabla p}{\rho} + \nu \nabla^2 \vec{u} + \vec{f} \quad \text{on } D \subset \Omega \tag{2.30}$$

where ν $[cm^2/s]$ is called kinematic viscosity and μ is the dynamic viscosity $[Pa \cdot s]$.

2.1.3 The Navier-Stokes Equations

Putting together the results found in Sections 2.1.1 (Equation 2.10)and 2.1.2 (Equation 2.30), we get the Navier–Stokes equations for an incompressible and Newtonian fluid in vector form, with a constant density ρ $[g/cm^3]$, and a constant kinematic viscosity ν $[cm^2/s]$:

$$\begin{cases} \dfrac{\partial \vec{u}}{\partial t} + (\vec{u} \cdot \nabla \vec{u}) = -\dfrac{\nabla p}{\rho} + \nu \nabla^2 \vec{u} + \vec{f} \\ \nabla \cdot \vec{u} = 0; \end{cases} \tag{2.31}$$

on $D \subset \Omega$ and for $t \geq 0$; where Ω is a region of three-dimensional space, where the fluid moves, and D is a volume in Ω.

The first equation represents conservation of linear momentum. It is a vector equation formed by three differential equations, one for each component of the velocity. The second is a scalar equation that represents conservation of mass, also refers to incompressibility constraint; in fact for an incompressible and homogeneous fluid, the density is constant in time.

We analyze different terms that appear in the equations:

1. $\vec{u}$ $[cm/s^{-1}]$, is a vector that represents the velocity of one point in space; it depends on the position and time.

2. $\partial \vec{u}/\partial t$, represent the unsteady acceleration.

3. $\vec{u} \cdot \nabla \vec{u}$, represent convective term, that is a spatial effect. Note that this term **is non linear in $\vec{u}$**, because of this the solution of the Navier-Stokes equations may develop instabilities, which are normally called turbulence. It is therefore natural to measure the importance of this term compared with the diffusive part given by $\nu \nabla^2 \vec{u}$. This information is provided by Reynolds number defined in Section 2.2.

4. $\nabla p/\rho$, $\vec{f}$ represent the action of forces.

To describe completely the motion of a fluid, in addition to the general Equations 2.31, we need to know the behavior of the physical quantities at the boundary of the domain filled by the fluid, in particular because the equations are second order in space it needs two boundary conditions. In this case we divide the boundary in two parts: Γ_D and Γ_N such that $\Gamma_d \cup \Gamma_N$, where in the first we apply the Dirichlet condition and in the second Neumann condition:

$$\begin{cases} \vec{u}(x,t) = \vec{\varphi}(x,t) \\ \nu(\nabla \vec{u}) \cdot n - pn = \vec{\psi}(x,t) \end{cases} \tag{2.32}$$

where φ and ψ are two vector functions assigned. We need also to prescribe the initial status of the fluid velocity because N-S is unsteady:

$$u(x,0) = u_0(x) \quad \forall x \in \Omega$$

2.1.4 Non-linearity

The Navier–Stokes equations are nonlinear partial differential equations. The non-linearity is due to convective term. It is important to highlight that any convective flow, whether turbulent or not, will involve non-linearity. Due to the non linearity of the equations finding an analytic solution is a hard task. Indeed the Clay Mathematics Institute has called this one of the seven most important open problems in mathematics and has offered a US $ 1,000,000 prize for the proof of uniqueness or a counter-example. However in some cases the equations can be simplified to linear equations and in this case we can find a uniqueness solution.

2.2 The Reynolds Number

The Reynolds number is a dimensionless number, that in an internal flow of velocity $\vec{u}$, within a geometry (es pipe or vessel, etc) of characteristic dimension L is given by

$$Re = \frac{\rho \vec{u} L}{\mu} \tag{2.33}$$

where μ is the dynamic viscosity of the Newtonian fluid. The value of the Reynolds number depends on the choice of the reference length and velocity. Usually, L can be taken as the diameter or as some other large-scale length related to, such as the width of a channel. The choice of $\vec{u}$ depends on the type of force acting on the flow. Various choices of L and $\vec{u}$ can be appropriate for a given flow, leading to various definitions of the Reynolds number. Re gives a measure of the ratio of inertial forces to viscous forces

$$Re = \frac{\text{inertial} \quad \text{forces}}{\text{viscous} \quad \text{forces}}. \tag{2.34}$$

It consequently quantifies the relative importance of convective flow than diffusion one, these for given flow conditions. Since the Re is a measure of inertial forces to viscous forces, its value characterize different flow regimes:

- Laminar

- Turbulent

Laminar flow occurs at low Reynolds numbers, where viscous forces are dominant. While turbulent flow occurs at high Reynolds numbers and is dominated by inertial forces, vortices and other flow instabilities.

2.2.1 Scaling Equations

It is common in physics to rewrite the equations describing a phenomenon in scaling form, i.e a form independent of the system of units. Scaling is a technique used to estimate the order of magnitude of the various terms in equations. It is useful to determine which terms are the most important for a specific problem, i.e it says us something about the importance of the specific terms in relation to other terms in the equation.

Now we derive the nondimensional form of the Navier-Stokes equations, starting from Equation 2.31. It should be noted that this step is not required for the solution of the flow problem but makes the setting of the problem and subsequent analysis more convenient. The following set of non-dimensional variables is used:

$$\begin{aligned} u^* = \frac{u}{u_R}; \quad t^* = \frac{t/u_R}{L_R}; \quad p^* = \frac{p}{p_R} \\ x^* = \frac{x}{L_R}; \quad y^* = \frac{y}{L_R}; \quad z^* = \frac{z}{L_R} \end{aligned} \tag{2.35}$$

where u_R, L_R, p_R, t_R, and f_R are, respectively, the characteristic velocity, length, pressure, time and force for the flow. We will choose, for example, for L_R the diameter of the volume filled by the fluid and for u_R the mean sectional velocity of the fluid. While for the other quantity we choose:

$$t_R = L_R \vec{u_R}; \quad P_R = \rho \vec{u}^2; \quad \vec{f_R} = \rho L_R / t_R^2 \tag{2.36}$$

The Navier stokes equation can be rewritten as:

$$\begin{cases} \dfrac{\partial \vec{u_R}}{\partial t_R} + (\vec{u_R} \cdot \nabla \vec{u_R}) = -\nabla p_R + \dfrac{1}{Re} \nabla^2 \vec{u_R} + \vec{f_R} \quad \text{on } D \subset \Omega \\ \nabla \cdot \vec{u_R} = 0 \quad \text{on } D \in \Omega \end{cases} \tag{2.37}$$

Where $Re = \vec{u}_R L_R / \nu$ is the Reynolds number. From the Equations [2.37] we deduce that the flow now only depends on one parameter: Re.

2.3 The Hagen-Poiseuille flow

In the Section [2.1.4], we said that the main issue, in solving N-S equations, lies in the non-linear convective term, that makes it difficult to determine analytical solution. In some cases, the non-linear terms can be neglected and it is possible to determine the exact analytical solutions. This approach is referred to the case of laminar flows since the random nature of the turbulent velocity in this case, makes it impossible to find the analytical solution.

Among the cases that have analytical solution, we will treat the Poiseuille flow.

The Hagen- Poiseuille flow was experimentally derived independently by Gotthilf Heinrich Ludwig Hagen in 1839 and Jean Louis Marie Poiseuille in 1838, and published by Poiseuille in 1840 and 1846.

2.3.1 Laminar Flow Between Infinite Parallel Plates

We assume that flow is:

- Steady, it means that the characteristic quantities of the system (like velocity,pressure, ...) are unchanging in time;
- Laminar, it occurs when a fluid flows in parallel layers.

Consider the flow between two infinite parallel plates at distance 2h and without external forces. We choose the frame of reference with the x axis that passes through the axis of

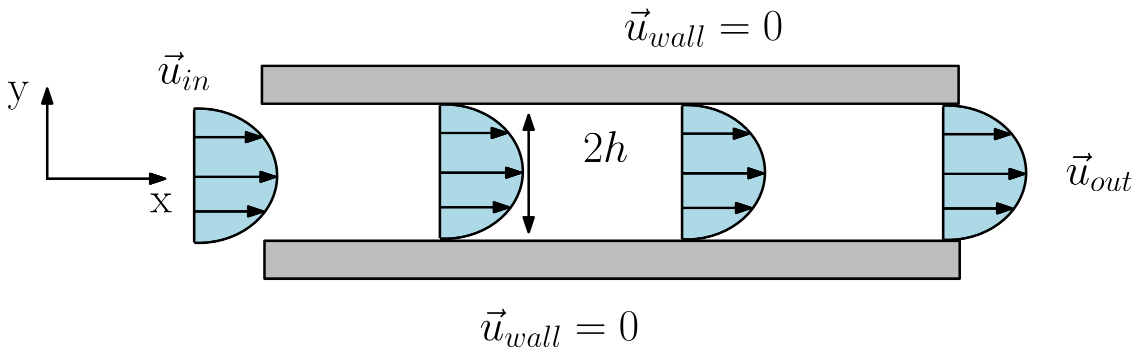

Figure 2.5: Flow between two parallel plates

symmetry of the system Figure 2.5. A pressure gradient G is applied between the two ends and we assume that the higher pressure region is on the left and the lower on the right, such that dp/dx is negative. The fluid velocity is directed to the right.

We are dealing with viscous flow, it means that on the plates both tangential and normal velocities must be zero, this condition is called **no-slip condition**.

The flow moves parallel to the plates (from left to right) and its has only the component along x different from zero.

Due to structure of the system we have:

$$\vec{u}(x, y) = (u_x(x, y); 0) \tag{2.38}$$

Because the plates are assumed infinite and the flow is steady, from the incompressibility constraint, it follows that u_x is only function of y:

$$\frac{\partial u_x}{\partial x} = 0 \tag{2.39}$$

The Navier- Stokes equations, written for each component, reduce to:

$$\begin{cases} -\dfrac{\partial p}{\partial x} + \mu \dfrac{\partial^2 u_x}{\partial y^2} = 0, \\ -\dfrac{\partial p}{\partial y} = 0 \end{cases} \tag{2.40}$$

which yields $p = p(x)$.

$$\frac{\partial p}{\partial x} = \mu \frac{\partial^2 u_x}{\partial y^2} \tag{2.41}$$

this is equal to the pressure drop by unit length (G/L). Integrating twice upon y, we find a possible solution of the System 2.40:

$$\begin{cases} p(x,y) = \dfrac{G}{L} x, \\ u_x(x,y) = \dfrac{1}{\mu} \dfrac{dp}{dx} + c_2 y + c_3. \end{cases} \tag{2.42}$$

By applying the no-slip conditions on the wall, we have:

$$\begin{aligned} u_x(-h) &= 0 \\ u_x(h) &= 0 \end{aligned} \tag{2.43}$$

We can determine the constants c_2, c_3, and substituting this value in the Equation 2.42, we obtain:

$$\begin{cases} p(x,y) = \dfrac{G}{L} x, \\ u_x 1(x,y) = -\dfrac{Gh^2}{2\mu L}(1 - \dfrac{y^2}{h^2}), \end{cases} \tag{2.44}$$

The flux problem is given by:

$$Q = \int_{-h}^{h} u_x(y)\, dx \tag{2.45}$$

that is:

$$Q = -\frac{2}{3} \frac{Gh^3}{L\mu} \tag{2.46}$$

Therefore, for a given flux Q, the flux problem is given by:

$$\begin{cases} p(x,y) = -\dfrac{3}{2}\dfrac{Q\mu}{h^3}x, \\ u_x(x,y) = \dfrac{3}{4}\dfrac{Q}{h}(1-\dfrac{y^2}{h^2}). \end{cases} \tag{2.47}$$

2.3.2 Poiseuille Flow In A Cylindrical Tube

Consider the flow of a fluid does:

- Laminar
- Steady ($\partial \vec{u}/\partial t = 0$)
- Axisymmetric ($\partial \vec{u}/\partial \theta = 0$)

through a tube of length L and radius R. A gradient of pressure G is applied between the inlet and the outlet and no-slip conditions are applied on the walls. Because the geometry of the problem, it is convenient to rewrite the problem in cylindrical coordinates (r, θ, z).

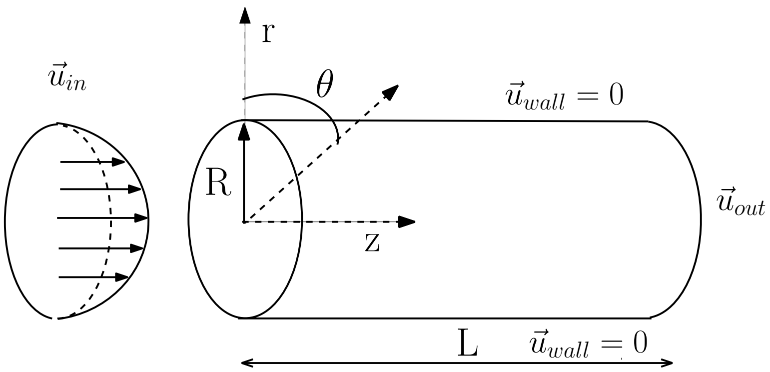

Figure 2.6: Geometry of the 3D problem

Due to the flow is laminar (namely the stream lines are parallel like Figure 2.6) $u_r = u_\theta = 0$, it means that the only no zero component of the velocity $\vec{u}$ is $u_z(r\theta, z)$. For the stationarity and axisymmetrial we have that $\partial u_z/\partial t = \partial u_z/\partial \theta = 0$; furthermore from the incompressiblility constraint, $\partial u_z/\partial z = 0$, we deduce that u_z is only function of r. The Nave-Stokes equations, in this case, are:

$$\begin{cases} \dfrac{\partial p}{\partial z} - \dfrac{\mu}{r}\dfrac{\partial}{\partial r}\dfrac{r\partial u_z}{\partial r} = 0 \\ \dfrac{\partial p}{\partial r} = \dfrac{\partial p}{\partial \theta} = 0 \end{cases} \tag{2.48}$$

Since p is only function of z it follows that:

$$\frac{\partial p}{\partial z} = \frac{G}{L} \tag{2.49}$$

A possible solution for the system above is:

$$\begin{cases} p(x,y) = \dfrac{G}{L}; \\ u_z(r) = c_1 r^2 + c_2 log(r) + c_3. \end{cases} \tag{2.50}$$

Since u_z is continuous $c_2 = 0$. The other constants can be found with slip condition. We obtain:

$$\begin{cases} p(x,y) = \dfrac{G}{L} z, \\ u_z(x,y) = -\dfrac{GR^2}{4\mu L}(1 - \dfrac{r^2}{R^2}). \end{cases} \tag{2.51}$$

The flux problem is given by

$$Q = \int_0^{2\pi} \int_{-0}^{R} u_z(r)\, dr d\theta \tag{2.52}$$

From it:

$$Q = -\frac{\pi G R^4}{8L\mu} \tag{2.53}$$

The flux problem is given by:

$$\begin{cases} p(x,y) = -\dfrac{8Q\mu}{\pi R^4} z, \\ u_z(x,y) = \dfrac{2Q}{\pi R^2}(1 - \dfrac{r^2}{R^2}). \end{cases} \tag{2.54}$$

Chapter 3

CFD:Computational Fluid Dynamics

Computational fluid dynamics, usually abbreviated as CFD, is a branch of fluid mechanics that uses numerical methods and algorithms to solve and analyze problems that involve fluid flows. Computers are used to perform the calculations required to simulate the interaction of liquids with surfaces defined by boundary conditions. With high-speed supercomputers, better solutions can be achieved. In the following section, the instruments used to generate the mesh, to simulate blood flow and to analyze the results are presented .

3.1 FEM: Finite Elements Method

The mathematical model we have briefly illustrated in the previous section can not in general be solved analytically, apart from simple case. Thus we have to resort to numerical techniques to find approximated solutions. The model that we have presented is based on partial differential equations:

$$\begin{cases} \dfrac{\partial \vec{u}}{\partial t} + (\vec{u} \cdot \nabla \vec{u}) = -\dfrac{\nabla p}{\rho} + \nu \nabla^2 \vec{u} + \vec{f} \quad \text{on } D \in \Omega \\ \nabla \cdot \vec{u} = 0 \quad \text{on } D \in \Omega \end{cases} \tag{3.1}$$

we have to resolve a time-dependent problem. In this case we need to discretize the time and for each time we have to solve numerically the N-S. For the solution of Navier-Stokes equations we use method that from the knowledge of the previous solutions builds the approximations u_h^{n+1} at time t^{n+1}. For each time the solution of the N-S is found using a common techniques based on the discretization of the physical domain Ω in elements of simple shape and finite size(like a grid), which constitute the computational mesh. In numerical techniques the solution u is replaced by an approximation u_h which depends on a finite number of parameters typically the values of u_h at the nodes of the grid.

There are many programs to generate mesh some open-source some not. In this thesis we will use open-source software, in particular we chose to work with program like Netgen or Vmtk that in addition to the mesh of the domain allow us to create or extrapolate (es from image) the computational domain.

3.1.1 Pre-Processing: Mesh

NETGEN

NETGEN was developed mainly by Joachim Schöberl within project grants from the Austrian Science Fund FWF (Special Research Project "Numerical and Symbolic Scientific Computing", Start Project "hp-FEM) at the Johannes Kepler University Linz. Netgen is a multi-platform automatic mesh generation tool written in C++ capable of generating meshes in two and three dimensions; in particular it generates triangular or quadrilateral meshes in 2D, and tetrahedral meshes in 3D. The input for 2D is described by spline curves, and the input for 3D problems can be defined by Constructive Solid Geometry (CSG), the standard STL file format. NETGEN provides modules for automated mesh optimization and hierarchical mesh refinement.

VMTK - The Vascular Modeling Toolkit

VMTK (www.hpfem.jku.at/netgen/)is a collection of libraries and tools for 3D reconstruction, geometric analysis, mesh generation and surface data analysis, from biomedical images. It is based on two libraries: VTK (the Visualization Toolkit) and ITK (the Insight Toolkit). This software was created by Luca Antiga (Unit of Medical Imaging, Department of Biomedical Engineering, Mario Negri Institute) and David Steinman (Biomedical Simulation Laboratory, Mechanical and Industrial Engineering, University of Toronto, Canada) on the basis of other open-source libraries: VTK, that provides tools for processing surfaces allowing for example operations of "cutting" and smoothing the surface; and ITK library, that provides the basic tools needed to perform the segmentation of images.

3.1.2 Solver: LifeV

LifeV (www.lifev.org) is a finite element (FE) library , written in C++, providing implementations of mathematical and numerical methods. It was born from the collaboration between four institutions: École Polytechnique Fédérale de Lausanne (CMCS) in Switzerland, Politecnico di Milano (MOX) in Italy, INRIA (REO, ESTIME) in France and Emory University (Sc. Comp) in the U.S.A.

The process to launch simulations using LifeV, needs the generation of a folder where we put specific files, which are:

- Mesh File (generate during pre-processing)
- Inlet_flow.dat; it is a text file that contains a column vector of elements, each of which is a component of the flow vector acquired at a precise moment of the cardiac cycle
- Data; it is a text file that is read by blood flow and contains all the features of the numerical model, the characteristics of the computational domain, the boundary conditions necessary to the resolution of the numerical problem, the parameters of material, etc.
- solverOption.xme; it is an executable that contains the information necessary to launch bloodflow.
- bloodflow.exe; it is written in C++, is the executable, which is able to solve the problem of fluid-structure interaction.

The output of lifeV is a series of file represent the solution of our problem for each step, that can not be analyzed as they are, but must be further processed through another executable, it generates a file containing the results of the simulation, readable with Paraview

3.1.3 Pre-processing: Paraview

ParaView (www.paraview.org) is an open source multiple-platform application for interactive, scientific visualization. It is an application built on top of the Visualization Tool Kit (VTK) libraries. Paraview allows the visualization of three-dimensional geometries and the execution of a large number of analysis through the use of filters, some already present in the software and executable by the tools bar, others imported from the outside, and still others created manually within the software.

3.2 Benchmark

We begin studying the flow field in simple models of the vessel geometry, a tube, where we will apply the Poiseuille flow.

During this study we will see what are the basic steps of the analysis and what factors influence the results.

The Navier-Stokes equations for incompressible an Newtonian flow are:

$$\begin{cases} \dfrac{\partial \vec{u}}{\partial t} + (\vec{u} \cdot \nabla \vec{u}) = -\dfrac{\nabla p}{\rho} + \nu \nabla^2 \vec{u} + \vec{f} \\ \nabla \cdot \vec{u} = 0 \end{cases} \tag{3.2}$$

In some cases, the non linear terms can be neglected and it is possible to determine the exact analytical solutions. This approach is always referred to the case of laminar flows.

In the next section we will compute analytic and numeric solutions

3.2.1 Analytical Solution For Poiseuille flow

In Section 2.3, page 18, we find the analytical solution of Poiseuille flow, for a given flux Q; now we implement it by Matlab (Matrix Laboratory):

$$\begin{cases} p(x, y) = -\dfrac{8Q\mu}{\pi R^4} z, \\ u_z(x, y) = \dfrac{2Q}{\pi R^2}(1 - \dfrac{r^2}{R^2}). \end{cases} \tag{3.3}$$

for a cylinder of radius R=0.1 cm and long L=10. We set the flux Q=1.8 m^3/s, while for the density and viscosity we use typical values of the blood, 1.06 g/cm^3, 0.04 g/cm respectively.

The solutions for velocity and pressure, calculated for a generic section of the cylinder, are shown below: The Figure 3.1 represents the linear gradient of pressure G applied between the

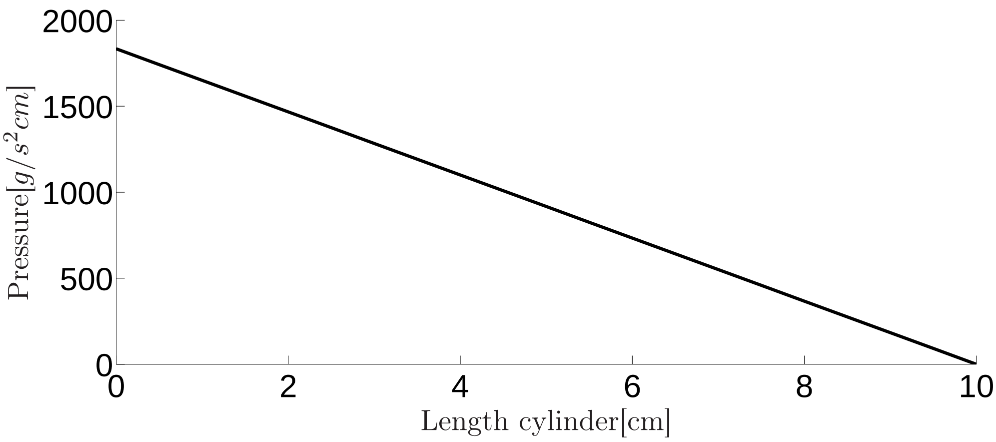

Figure 3.1: The graph shows the linear pressure relation.

inlet and the outlet.

In the Figure 3.2 we can see that the flow velocity is parabolic and respects the slip-condition, in fact in the cylinder wall the velocity is zero an in the center is maximum.

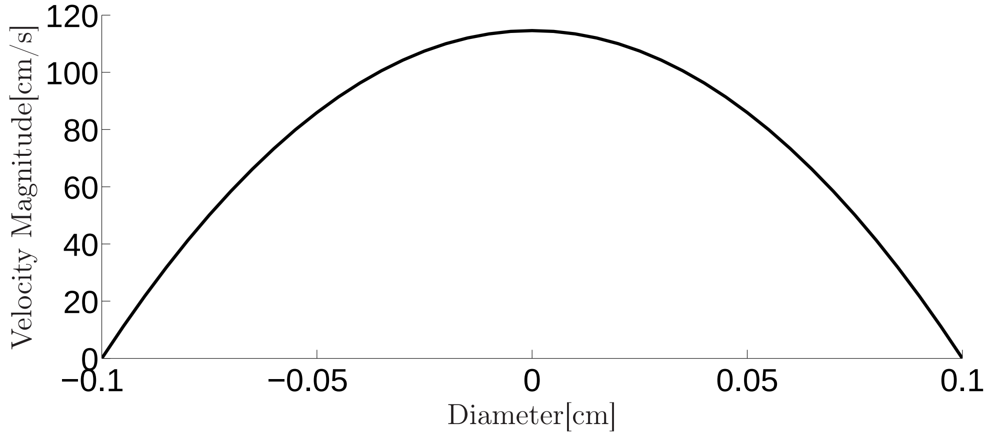

Figure 3.2: The analytic velocity for the Poiseuille Flow is parabolic. It is maximum in the center of the cylinder and respects the slip-condition, i.e the velocity is null in the wall.

3.2.2 Numerical Solution For Poiseuille Flow

The numerical solution is calculated by applying several steps:

- Building a solid geometry (CSG), to determine the functional domain;
- Generating mesh;
- Simulating the Poiseuille flow through the cylinder;
- Analyzing data.

Geometry And Mesh

The simplest model of a vessel is a cylinder, so the first step is to build a solid geometry. We realize it by the method of *Constructive Solid Geometry (CSG)* and NETGEN will be used to generate the mesh.

In the CSG technique a solid is defined by the Eulerian operations (union, intersection and complement) applied to primitives. The CSG file is saved in the .geo format, a particular format that can be read by **NETGEN**. After creating the cylinder, we upload it on NETGEN and mesh it, as described in section [1.2.1]

In this discretize domain we simulate blood flow by the finite element library *LifeV*.

Netgen allows to save the mesh in different format, among *.vol*, that can be given in input to Life V to processes it.

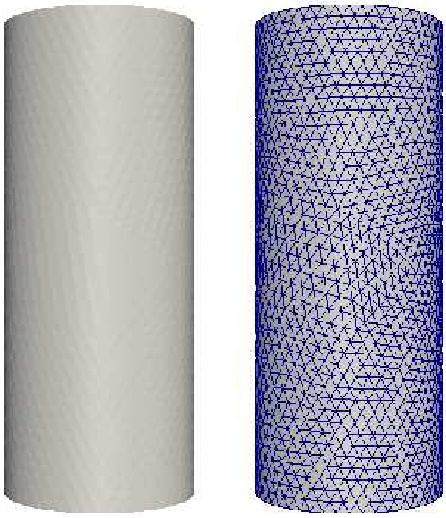

(a) CSG (b) Mesh

Figure 3.3: Image of the geometry and the mesh realized by NETGEN. The mesh is formed by 70144 elements.

Analyzing Data

Finally, the data obtained is analyze by *Paraview*. For the cylinder we examine the trend of the pressure and the velocity, to see if the found data approximately mach those found analytically.

The Figure[3.4] shows the results.

On the left is depicted the linear gradient of pressure G applied between the inlet, where the value of pressure is maximum, and the outlet, where is minimum. While on the right is shows the trend of the velocity, it is maximum in the center of the cylinder and decreases with the increase of the radius, and becomes zero on the wall, this indicates that the no-slip condition is observed.

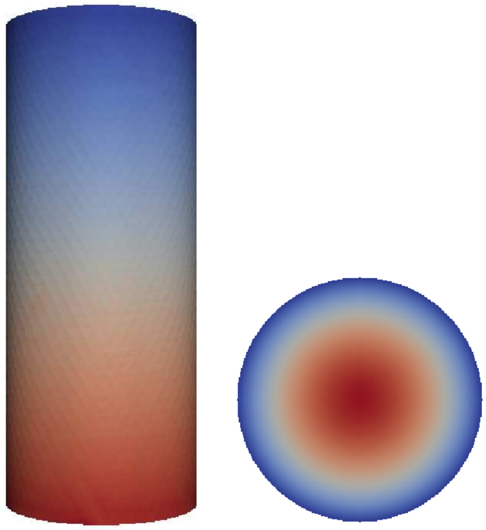

(a) Numeric Pressure (b) Numeric Velocity

Figure 3.4: Numerical results for pressure and velocity of Poiseuille flow through the cylinder. Qualitatively, we can say that the numerical results agree with the analytical ones. In the figure on the left is showed the trend of the pressure, it linearly along the cylinder. In the figure on the right is shown the velocity trend in a cross-section, it is parabolic: maximum at the center and nothing in the wall

3.2.3 Compare Results

For the geometry described in Section 3.2.1, we want to compare the results of the velocity, found analytically, implementing the Equation 3.3, with those found numerically in the Section 3.2.2 by LifeV. Before the last can be used must be treated with Paraview; in particular we select a general section of the cylinder, with the command "slide"; after that, applying the filter "plot on intersection curves", we can visualize and save the following variables of the system as a function of the diameter:

- coordinates of each node (x, y, z),which is located along the diameter considered;
- components of velocity vector (u_1,u_2,u_3).
- pressure

We load the velocity data on Matlab.

For each point (x,y,z) included in the section we can calculate:

- the magnitude of numerical velocity ($\vec{u}_{num}$):

$$\vec{u}_{num} = \sqrt{u_1^2 + u_2^2 + u_3^2} \tag{3.4}$$

- the analytical velocity ($\vec{u_{an}}$) computed as:

$$\vec{u}_{an} = 2QR^2(1 - \frac{r^2}{R^2}) \tag{3.5}$$

where $r = \sqrt{x^2 + y^2}$ is the radial component of cylindrical reference system, R is the radius of the cylinder and Q is the volumetric flow rate.

In the Figure 3.5 we plot the analytical solution $\vec{u}_{an}$ (black) and the numerical one $\vec{u}_{num}$(red).

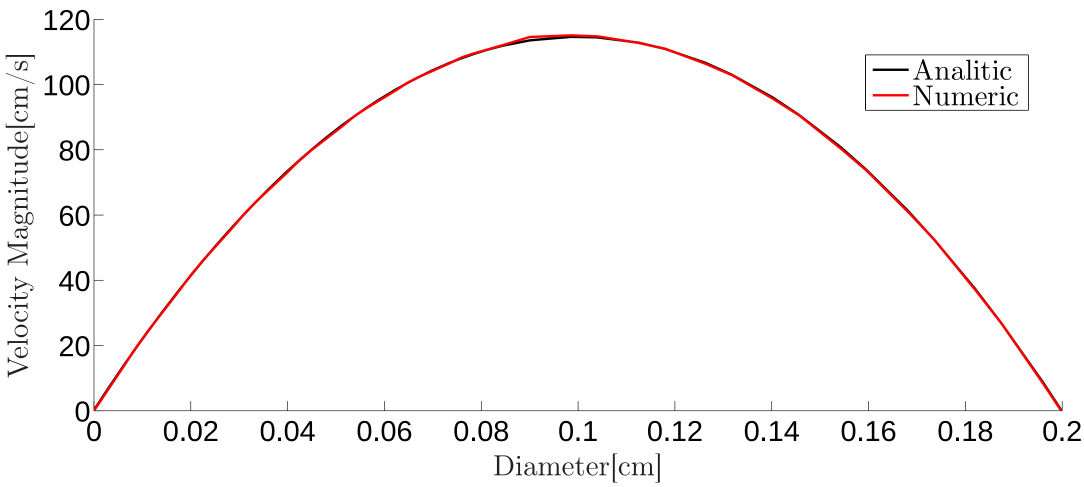

Figure 3.5: Compare analytical (red) and numerical (blue) solution. The graft demonstrates that, for the Poiseuille flow the numerical solution approximates well the analytical one

The figure 3.5 shows that the numerical solution is approximately equal to analytical solution. The differences are not because the numerical solution is different from analytical, or wrong, it depends on several parameters, including how good are the numerical results. In Section 3.3, we will prove that the numerical results depend on how fine is the mesh; in particular **more the mesh is fine, more the numerical solution approaches the analytical**.

3.3 Convergence Order

It is a good idea, when using a numerical code, to perform a test on a case that has analytical solution to verify that there are no big error. To evaluate the convergence order, we generate several meshes with different number of elements for the cylinder in Figure 3.9a, in which we will implement the Poiseuille problem (which presents analytical solution). In particular we will note how the error of the numerical solution decreases as increases the number of the elements of the mesh.

3.3.1 Error Estimate

Each numerical method utilizes to the resolution of a problem provides an approximate solution. The approximation can be estimated by a global parameter called error. If we consider a problem that is known, the exact solution a priori, $\vec{u}$, the error in define as:

$$e = \int_{-R}^{R} \frac{e_i}{N}\, dr \tag{3.6}$$

where e_i is the error carries out in each node, we calculate it by doing the differences between the exact solution and the approximated one, in correspondence of each nodes. N represents the number of the nodes of the mesh in a section of the cylinder, and normalizing with respect v_{numi}, as follows:

$$e_i = \frac{|u_{numi} - u_{ani}|}{u_{numi}} \quad \text{with} i \in N \tag{3.7}$$

then the error can be calculated as:

$$e \simeq \sum_{i=1}^{N} \frac{e_i}{N} \tag{3.8}$$

For the CSG in Figure 3.9a, we generate four meshes with the following number of elements. Each mesh was generated by applying the refinement to the previous one:

Mesh	1	2	3	4
# elements	137	1096	8768	70144

Table 3.1: Number of elements for the four mesh realized with Netgen

Mesh 1

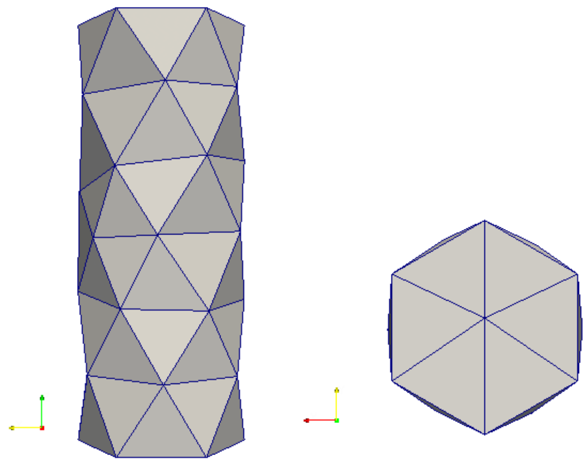

(a) Longitudinal section (b) Mesh Cylinder

Figure 3.6: Discretize domain, with 137 elements

Mesh 2

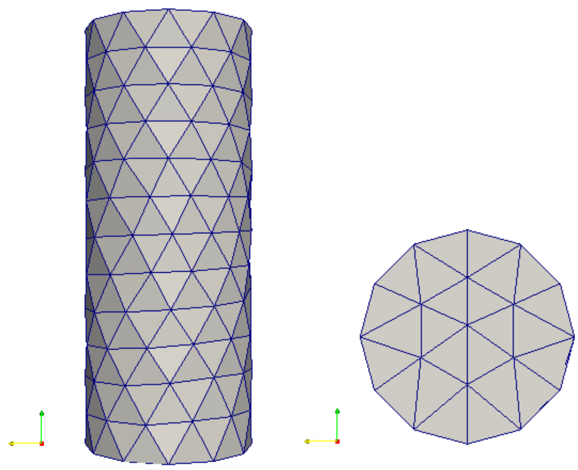

(a) Longitudinal section (b) Mesh Cylinder

Figure 3.7: Discretize domain, with 1096 elements

Mesh 3

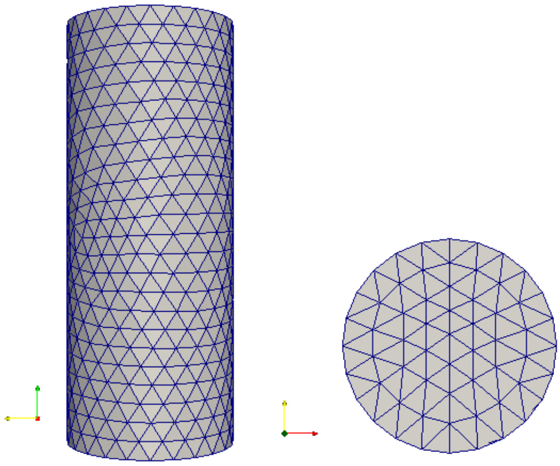

(a) Longitudinal section (b) Mesh Cylinder

Figure 3.8: Discretize domain, with 8768 elements

Mesh 4

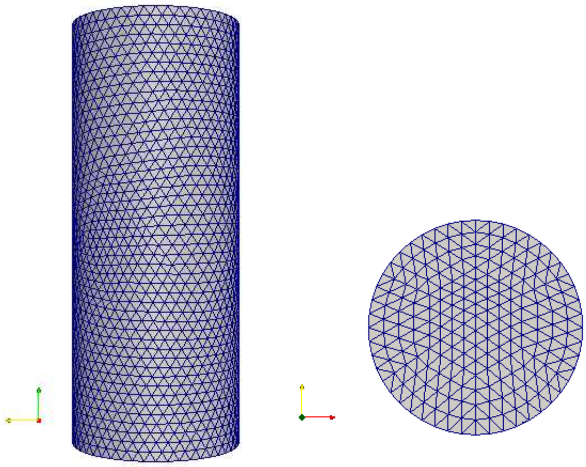

(a) Longitudinal section (b) Mesh Cylinder

Figure 3.9: Discretize domain, with 70144 elements

For each mesh, CFD analysis is performed using LifeV. The results are processed with Paraview as a Section [3.2.3], and from this data we can calculate the error, using the Equations[3.9].

In the Table [3.2], for each mesh, we report the results for the error.

To assess the convergence order of a numerical method, we have to evaluate the error in function of a parameter h, that indicates the finesse of the mesh used. Mathematically it means:

$$e = Ch^p \tag{3.9}$$

Mesh	# elements	error
1	137	0.334
2	1096	0.076
3	8768	0.066
4	70144	0.030

Table 3.2: Errors results. From the table we can see that the error made by approximating the analytical solution with the numerical one decreases with increasing fineness of the mesh

where p is the convergence order, while C is the accuracy constant of the solution: the smaller C,the more accurate is the solution.

To get the order of the error as a function of h, in an easy manner, it is recommended to represent the graphs on a logarithmic scale.

Applying the logarithm at the equation 3.9, we obtain:

$$log(e) = log(C) + plog(h) \tag{3.10}$$

The equation 3.9 becomes the equation of a straight line, with intercept $log(C)$ that represents the accuracy constant of the method used; while the slope p is the convergence order. In general, the slope p of a straight line is calculated as:

$$p = \frac{log(y_2) - log(y_1)}{log(x_2) - log(x_1)} \tag{3.11}$$

where $(x_2, y_2); (x_1, y_1)$ are two points of the straight line. Instead $log(C)$ is calculated as:

$$log(C) = log(e_1) - plog(h_1) \tag{3.12}$$

We can calculate p with the Equation 3.11:

$$p = \frac{log(e_i) - log(e_{i-1})}{log(h_i) - log(h_{i-1})} \tag{3.13}$$

recalling that each mesh is obtained by applying the refinement of the previous one, due to $h_i = h_{i-1}/2$, therefore, the denominator of the Equation [3.11] becomes $log(2)$.

Evaluating the Equation 3.11 at the data in the Table 3.3, we find that the line straight has three slopes:

p_1	2.13
p_2	0.20
p_3	1.13

Table 3.3: Slopes of the convergence order.

The graph in Figure 3.10 shows us that the line that represents the behavior of the error as a function of the elements number of the mesh, on a logarithms scale:

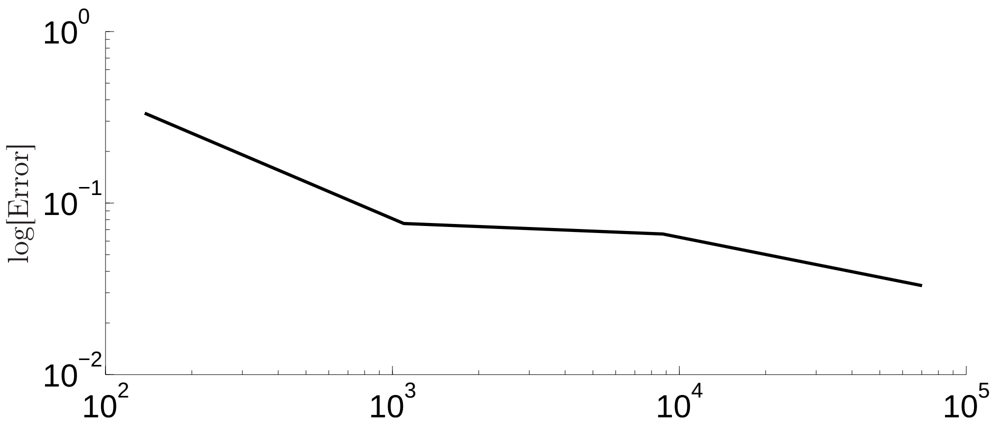

Figure 3.10: The figure represents the error Behavior on a logarithms scale. The curve has three slopes: in the first part of the convergence order is 2.13, this means that the error decreases rapidly to increase of the elements of the mesh; in the central part p = 0:13, from 1096 to 8768 mesh element, the error remains approximately constant. Finally in the last part we see that the error tends to zero with order of convergence equal to 1.13

From the graph 3.10, we can conclude that as the numbers of elements of the mesh increases, the error, in approximating the analytical solution with the numerical one, tend to zero.

3.4 Inflow

We continue our study of parameters that affect the flow. An interesting parameter to consider is the shape profile of the inflow, which can be:

- Flat

$$\begin{cases} \vec{u}_r = 0 \\ \vec{u}_\theta = 0 \\ \vec{u}_z(r) = Cost \end{cases} \tag{3.14}$$

- Parabolic

$$\begin{cases} \vec{u}_r = 0 \\ \vec{u}_\theta = 0 \\ \vec{u}_z(r) = \frac{2\vec{Q}}{\pi R^2}(1 - \frac{r^2}{R^2}) \end{cases} \tag{3.15}$$

The usual cylindrical geometry is considered:

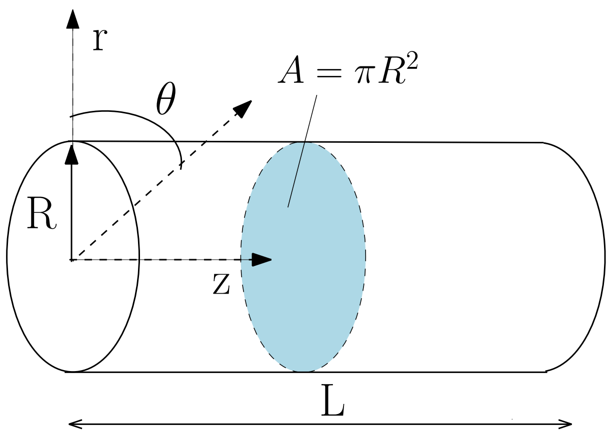

Figure 3.11: System Geometry

With the following features

- Diameter= 3.3 cm
- Length= 40 cm

In the geometry showed on the figure 3.11, we apply a steady flow $\vec{Q}$, that is to say a flow constant in time; constant in time does not mean that the flow is at rest, but that does not vary in time.

We chose a flow in such a way the value of the Reynolds number avoids the formation of turbulence.

$$Re = \frac{\rho \vec{u}_{avg} D}{\mu} \tag{3.16}$$

From the Reynolnds number we find the expression of the main velocity

$$\vec{u}_{avg} = \frac{Re\mu}{\rho D} \tag{3.17}$$

and from that we can calculate the flux like:

$$\vec{Q} = \pi R^2 \vec{u}_{avg} = \vec{Q} = \frac{2\pi\mu R_e R^2}{\rho} \tag{3.18}$$

Re	$\vec{u}$	$\vec{Q}$
500	5,71 cm/s	$\cong 50\ cm^3/s$

Table 3.4: Values inflow. This are chosen to avoid the formation of turbulence.

where $\vec{u}_{avg}$ is the average velocity, it is defined as the average velocity through a cross section. For fully developed laminar pipe flow, $\vec{u}_{avg}$ is half of maximum velocity. We choose values typical of the blood for the fluid dynamics constants:

- $\rho = 1,06\frac{cm}{s}$
- $\mu = 0.04\frac{g}{scm}$

Reynolds number is chosen about 500, for this value we will study either cases of shape inflow. As shown in the equation 3.18, we calculate the following values for the $\vec{Q}$ After doing these

calculations and the mesh geometry(see section), we simulate the steady flow for both values of profile shape by **LifeV**.

3.4.1 Flat Profile

Consider a **flat flow** entering a pipe, like in figure:

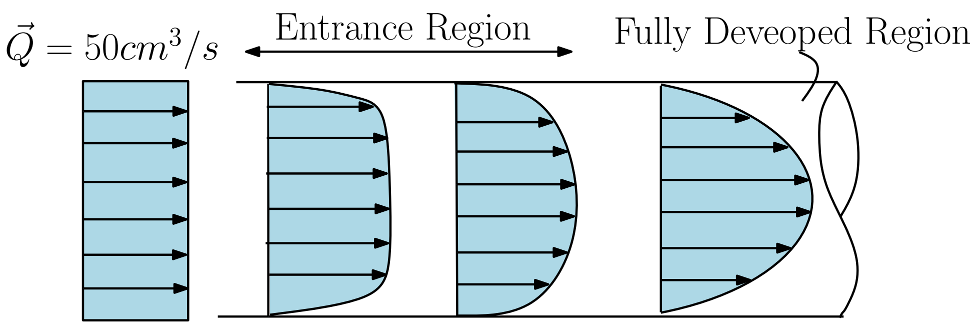

Figure 3.12: Inflow Velocity: Flat Profile. The diagram illustrates the entrance region and fully developed flow. When fluid enters a pipe its velocity profile is flat, i.e uniform across the pipe cross-section. At the entrance, near the wall, the flow is slowed due to the viscous forces and changes in the velocity profile take place, as long as the flow is not fully developed and there are no more changes. Now the flow is completely viscous. The entrance portion of the pipe, where the velocity profile is changing is called the entrance region, and the flow after that entrance region is called fully developed flow.

Let us think of the entering flow being uniform, so inviscid. As soon as the flow 'hits' the pipe many changes take place. Because of the **no-slip** condition, the fluid particles in the layer in contact with the surface of the pipe come to complete stop. Consequently the velocity components are zero on the wall. This layer also causes the fluid particles in the adjacent layer to slow down gradually. In fact we have a layer close to the wall where the velocity arise from zero at wall to a uniform velocity towards the center of the pipe. This layer is called the Boundary Layer. Viscous effects are dominant within the boundary layer. Outside this layer there is the inviscid core where viscous effects are negligible or absent. The boundary layer from the walls grows until the centre of the pipe. Once this takes place, inviscid core terminates and the flow is all viscous. The flow is now called a **fully developed flow**. The velocity profile in the fully developed laminar flow becomes parabolic, each fluid particle moves at a constant axial velocity along a streamline and the velocity profile $u_z(r)$ remains unchanged in the flow direction. There is no motion in the radial direction. There is no acceleration since the flow is steady and fully developed. The region from the pipe inlet to the point at which the boundary layer merges at the centerline is called Entrance Length. Denoted by Le, the entrance length is a function of the Reynolds Number of the flow $\frac{L_e}{D} \cong 0.06 Re_D$ [13], for this reason, in this case, we chose the length cylinder equal to 40 cm.

From the analysis of the simulation results we can observe that previously expounded. We consider two slides of our cylinder, one near the inflow and other outflow, and made plot of Magnitude velocity versus diameter:

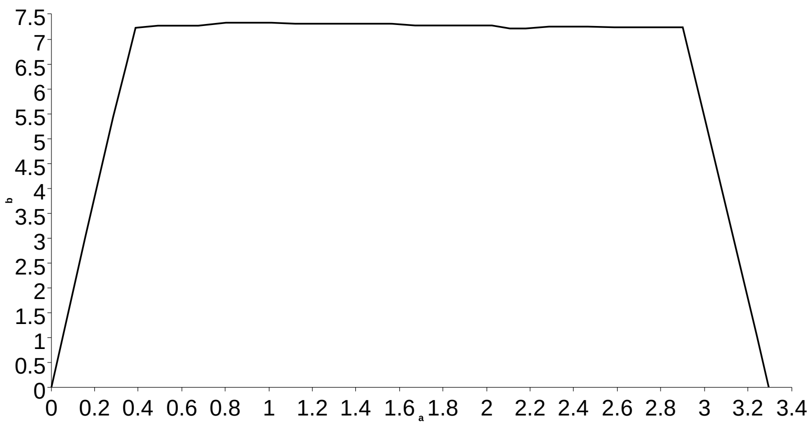

Figure 3.13: Inflow Flat Velocity. The data are taken at the enter of the cylinder. Because of this in the graph we begin to see the effects of the wall on the flow.

We can observe, that for a inflow flat flow, we find the solution of Poiseuille in outflow. In this case the outgoing solution is not fully developed because the simulation time or the cylinder length are too small. In the figure 3.15 we can see as time increases (i.e the number of cycles, we are considering the periodic solutions), the solution gets close to the analytical solution and becomes parabolic.

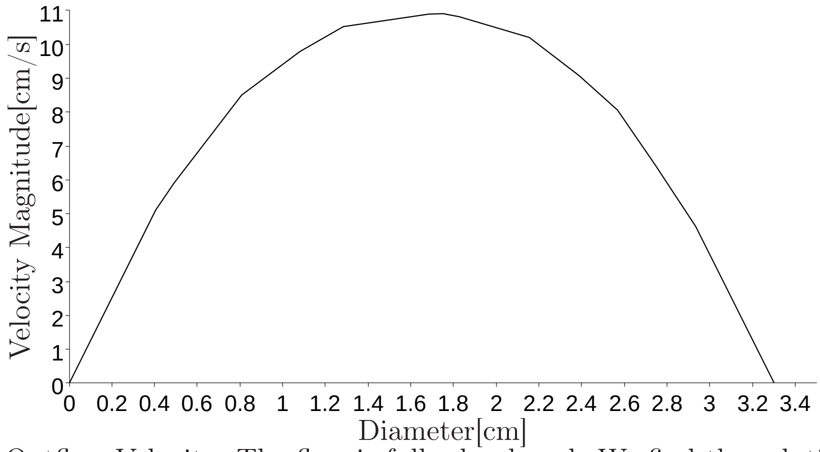

Figure 3.14: Outflow Velocity. The flow is fully developed. We find the solution of Poiseuille flow.

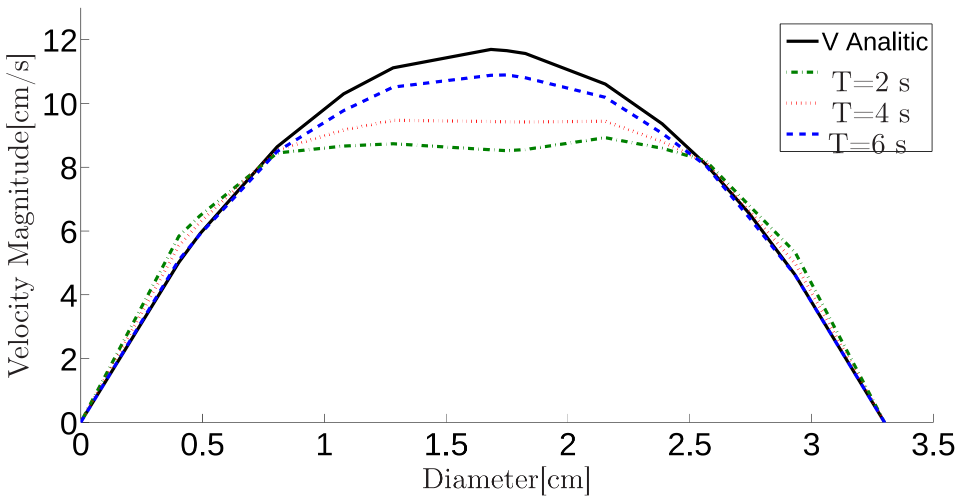

Figure 3.15: Compare velocity outflow, measured for six times with analytical solution.Tge graft shows that as time increases the numerical solution gets close to the analytical one and becomes parabolic.

3.4.2 Parabolic Profile

Also in this case we consider two slides of our cylinder, one near the inflow and other outflow, and made plot of magnitude of the velocity versus diameter:

In this case the shape inflow has the same form that we expect for the outflow, because the boundary Condition are respected (i.e $\vec{u}$ is zero in the wall). It follows that the solution develops in less time than the previous case and to develop does not need a minimum length. During this simulation we see that the analytical solution is well approximated by the numerical one (remember that the errors may be due to the choice of the mesh).

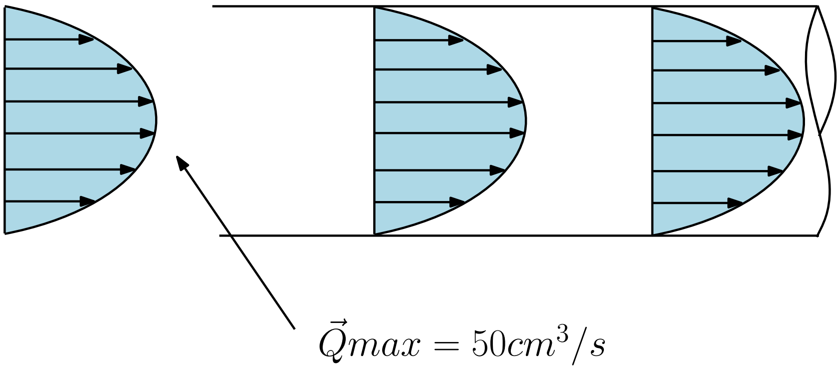

Figure 3.16: Parabolic inflow. The velocity profile does not change because the flow respects the boundary conditions

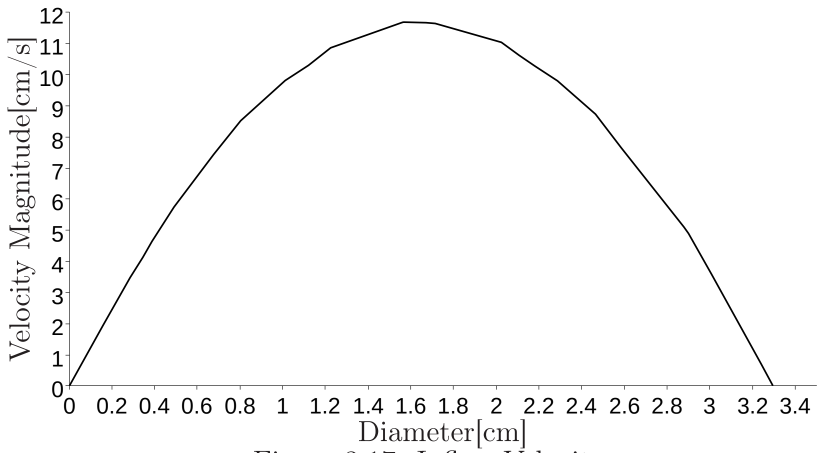

Figure 3.17: Inflow Velocity

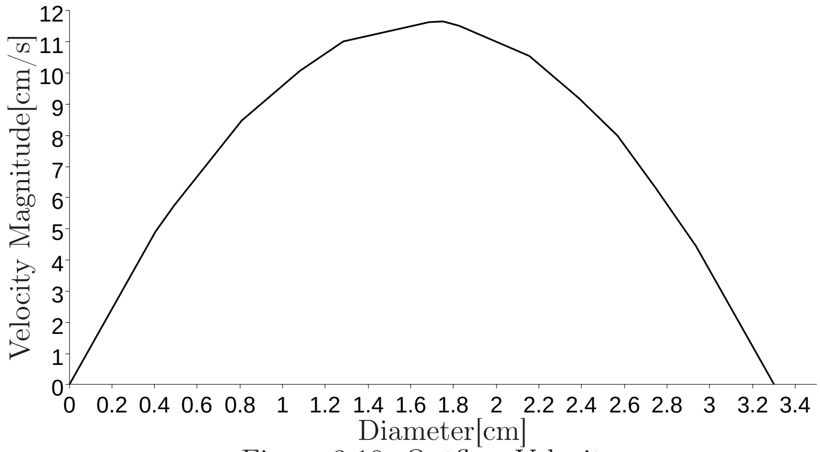

Figure 3.18: Outflow Velocity

Chapter 4

Flow in a curved pipe

Cardiovascular disease causes nearly half of all deaths in Europe and is the main cause of death. A lot of research has been done in order to prevent, diagnose and treat cardiovascular disease, but there are still a lot of gaps in our knowledge about it. One of the major problems is the complexity of the cardiovascular system. The vessels bifurcate, curve and taper, which make the analysis complex. In the previous sections we have dealt with the case of tube (i.e straight pipe) where (under appropriate conditions) we applied the Poiseuille flow. Because in this study we want to analyze the hemodynamics of the aorta, to measure and interpreter the flow dynamics in the complex geometry of the human aortic arch is important to understand the effects of curvature on the flow development.

In this chapter we would analyze the effects of curvature on the flow to uncover characteristic features of the relation between flow and vessel geometry using CFD analysis in a curved planar pipe, where the assumption of Poiseuille flow in not valid. The major difference between the flow in straight tubes and the flow in curved tubes is that the first generally is axisymmetric, while the further is not.

4.1 Geometry And Flow

When a fluid flows through a curved pipe of any cross-section it is observed that a secondary flow occurs in planes perpendicular to the central axis of the pipe. The secondary flow is imposed on the fluid due to centrifugal force. Because the centrifugal force is directly proportional to the axial velocity $\vec{F_c} = \rho\vec{u}^2/Rc$ (where $\vec{u}$ is the axial velocity, ρ the density and Rc the curvature radius), the fluid near the axis of the tube, that have the highest velocity value, is subjected to a centrifugal force larger than the fluid near the wall.

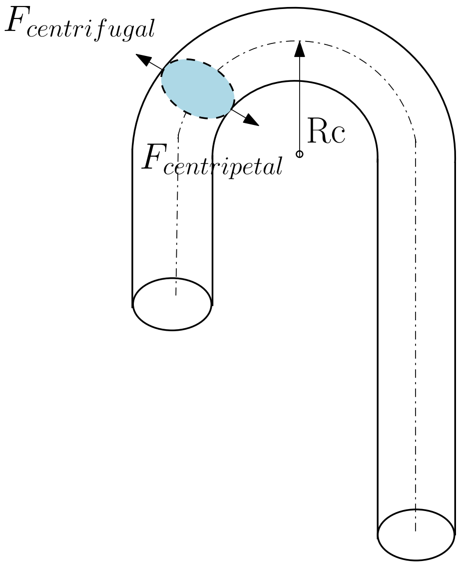

Figure 4.1: Representation of the centrifugal forced in a curved planar pipe.

To balance the centrifugal force on the fluid, due to its curved trajectory, there must be a pressure gradient across the pipe, the pressure being greatest at the outer wall of the pipe and least at the inner wall. The fluid near the top and bottom wall of the pipe is moving slower than that near the central plane, due to viscosity, and therefore requires a smaller pressure gradient to balance its reduced centrifugal force. Consequently a secondary flow occurs in which the fluid near the top and bottom walls of the pipe moves towards the central axis and the fluid near the central plane moves outwards.

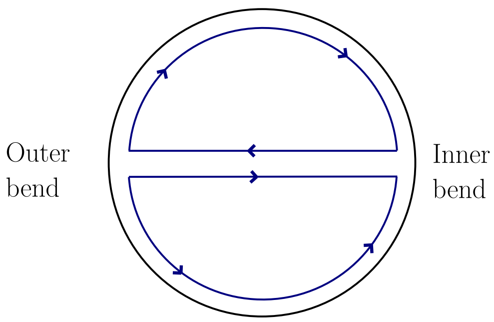

Figure 4.2: Secondary motion of the fluid in the curved. Due to the curvature a centrifugal force is generated. It does that the fluid near the outer and inner bend moves towards the central axis and vice versa.

This in turn modifies the axial velocity. Since fluid with a larger axial velocity moves outward, the maximum axial velocity moves outwards; while fluid with a smaller axial velocity are moving inwards and are thus decreasing the axial velocity on the inside of the curve.

The secondary flow gives rise to a C-shaped axial velocity profile with the maximum shifted

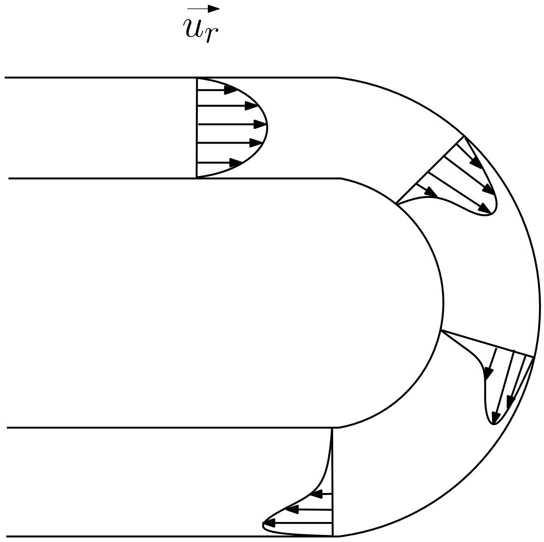

Figure 4.3: In correspondence of the curvature, the maximum axial velocity shifted towards the outer part of the curve due to the centrifugal force

to the outer curve and a minimum near the inner of the curve, how we can observe in Figure 4.3.

The fluid is constantly transported from the axis of the tube, where it has a high velocity, to the outer wall, where the velocity is low due to the viscosity, so retarded fluid is carried to the walls. The accumulation of the retarded at the walls results in a diminution of flux through the pipe.

Experimental investigations of the secondary flow were made by Eustice [6], he proved the existence of the secondary flow by performing an experiment where he injected ink into water flowing though a curved pipe.

The first theoretical analysis given by Dean for the case of an incompressible fluid in steady motion through a pipe of circular cross-section. In 1927, Dean was the first to find an analytical solution describing the steady flow of an incompressible fluid in curved tubes with a small curvature [19]. This analytical solution (valid only for Dean number$<$96) was based on the assumption that the secondary flow is just a small disturbance of the Poiseuille flow in a straight tube.

In 1928 Dean published another article, because he was not satisfied of the first [5]. He did not like his first approximation, which failed to show that the relation between the pressure gradient and the flow rate through a curved tube depends on the curvature.

4.1.1 Dean Number

The Dean number comes from the scaling of the Navier-Stokes equations, written in toroidal coordinates. This is a dimensionless number, defined as:

$$De = \sqrt{\frac{D}{2Rc}} Re_D \tag{4.1}$$

where D is the pipe diameter, Rc in the radius of curvature and Re_D is the Reynolds number based on **mean axial velocity** and d is the diameter of the pipe.

The Dean number can be interpreted as the ratio of the square root of the product of convective inertial forces,centrifugal forces and viscous forces :

$$De = \sqrt{\frac{D}{2Rc}} Re_D \quad \cong \sqrt{\frac{\text{centripetal} \quad \text{forces} \times \text{inertial} \quad \text{forces}}{\text{viscous} \quad \text{forces}}} \tag{4.2}$$

4.1.2 Numerical simulations of the flow in a planar curved pipe

We realized a planar curved pipe, of diameter equal to 5cm and radius of curvature of 6.5cm, via the method of CSG (Section [3.2.2]), combining a half toroid with two cylinders.

The mesh-grid was built dividing the fluid domain into 46092 tetrahedral cells by Netgen, see Figure 4.4:

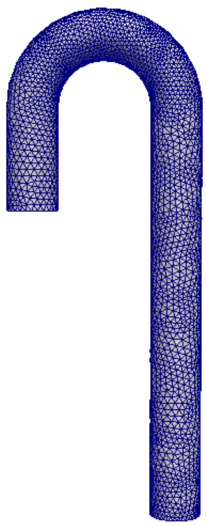

Figure 4.4: Mesh of the curve planar pipe consists by 66992 elements

In this domain, we have approximated the solution of the three-dimensional Navier Stokes equations for steady, parabolic, incompressible Newtonian flow in a curved pipe with the following features: where ρ is the curvature ratio, defines as:

D	Rc	δ	$\vec{u}$	Re	De
5 cm	$\cong 7cm$	0,73	2,5 cm/s	$\cong$ 335	200

Table 4.1: Features of the fluid flows in the curved pipe.

$$rho = \frac{d}{R_c} \tag{4.3}$$

The initial condition is null velocity. For the boundary conditions we set: a no-slip condition in the wall and a constant flux of 50 cm^3/s, with parabolic profile, in the inlet. The problem is solved over six cycle, in such a way that the results are not influenced by the initial condition and the boundary conditions. To performer the simulation we use LifeV (see Section 3.1.2) and to analyze it, we use Paraview (see Section 3.1.3) .

The results that we find, agree with the literature.

4.2 Steady flow In A Curved Pipe

We measure the axial velocity component at five cross-sections in the bend as show in Figure 4.5. In the Figure 4.5 the axial velocity distribution is given by isovelocity contours at three

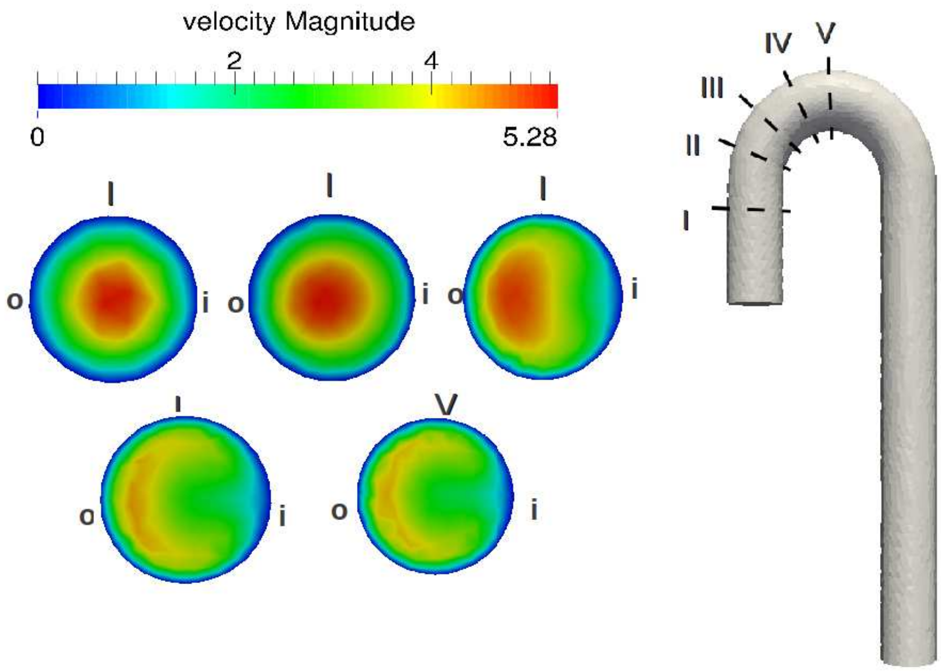

Figure 4.5: Qualitative trend of axial velocity [cm/s], shown for several cross-section. The figure shows thst the maximum of the axial velocity shifts towards the outer bend in the bend

cross-sections in the tube ($\theta = 0$, $\theta = \pi/4$, $\theta = \pi/2$, π). In Figure 4.5 I means inner wall of curvature and O outer wall of curvature. At $\theta = 0$ the axial velocity is parabolic, so without curvature we find the Poiseuille flow profile. Also observe that with the increase of the curvature, the centrifugal force raises so the peak velocity moves towards the outer wall of the tube. In figure 4.6 the development of the axial velocity in the plane of symmetry is given. At the first velocity profile, corresponding to $\theta = 0$, the influence of the curvature is

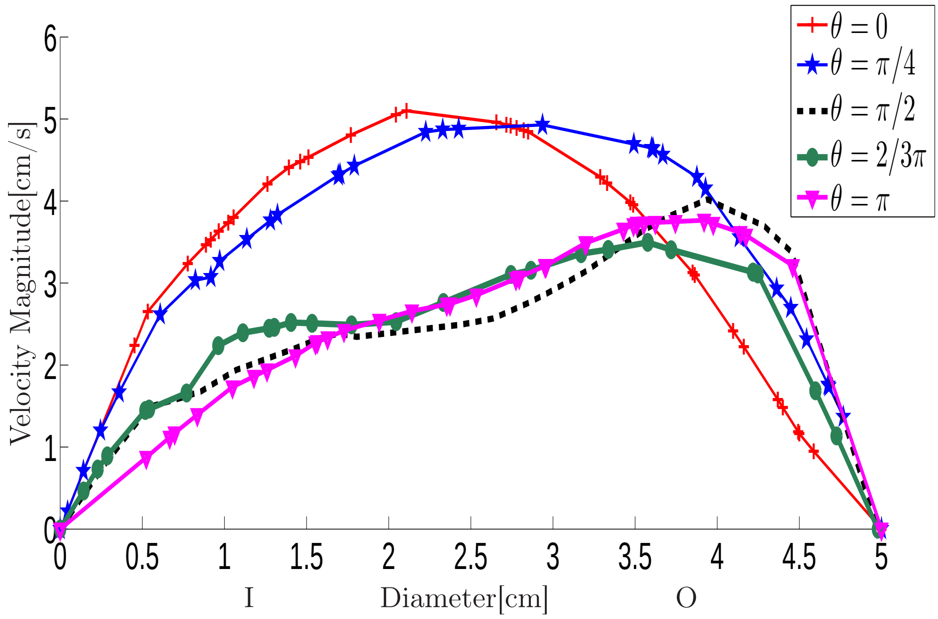

Figure 4.6: Analysis of the axial velocity [cm/s], in the plane of symmetry of the curved tube, for different bending angles. The graph shows that: the greater the angle of curvature, the more the maximum of the axial velocity is shifted towards the outer bend and it decreases. O,I denote outer and inner bend, respectively.

not visible, in fact, the solution is the same of the Poiseuille flow. At $\theta = \pi/4$ the maximum of the axial velocity profiles start to shift towards the outer bend. Furthermore it is evident that the magnitude of velocity decreases with the increase of curvature, due to the secondary flows, consequently the flow decrease. The calculations agree with the results found in the articles: [7], [12], [16], [8].

4.2.1 Secondary Flow

Secondary flows occur when there is a flow around a bend in a pipe. At the bend,the pressure can be described as follows:

$$p(r, \theta, z) = p_0(r, \theta) + \frac{G}{R} z \tag{4.4}$$

Where $p_0(r, \theta)$ is the pressure in the cross section of the tube, which is caused by the centrifugal forces and G/R is a pressure gradient constant in the axial direction, comparable to the

Poiseuille flow.

The pressure gradient require for the faster moving fluid near the center of the pipe to follow the curve of the bend is greater than that required for the slower moving fluid near to the wall. This results in the fluid near the center of the pipe moving toward the outside of the pipe and the fluid near the wall moving inwards (Figure 4.7). The figure shows our numerical

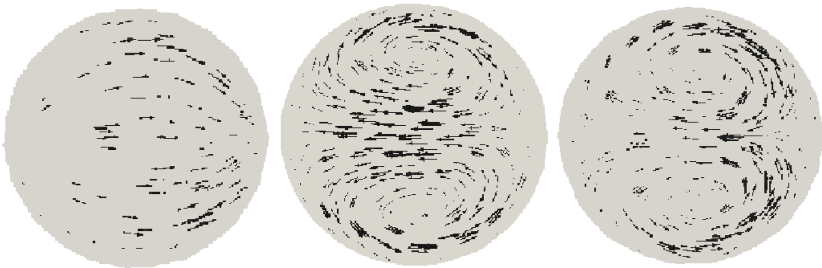

(a) $\theta = 0$ (b) $\theta = \pi/4$ (c) $\theta = \pi/2$

Figure 4.7: Secondary velocity vectors in the curved tube. At the entrance($\theta = 0$) the influence of the bend is very small. At $\theta \cong \pi/4$ a vortex has developed, which near the plane of symmetry is directed from the inner bend towards the outer bend and the upper wall from the outer bend back to the inner bend.At $\theta \cong \pi/2$ The secondary velocity are lower than $\theta \cong \pi/4$.

results, that were displayed in Paraview applying, fisrt the filter "surface vector", then the filter "glyph" filter at the velocity. At the entrance ($\theta = 0$) the influence of the bend is very small. At $\theta \cong \pi/4$ a vortex has developed, which near the plane of symmetry is directed from the inner bend towards the outer bend and the upper wall from the outer bend back to the inner bend.At $\theta \cong \pi/2$ the secondary velocity is lower than $\theta \cong \pi/4$.

4.2.2 Vorticity

We focused our attention on velocity. In many cases it is advantageous to interpreter the flow events in terms of vorticity. As can be seen in Section 4.2.1, in curved pipe, two symmetric vortices take place. To quantify these vortices, the vorticity $\vec{w}$ of the flow is determined. The vorticity of the flow is defined as the curl of the velocity $\vec{u}$:

$$\vec{w} = \vec{\nabla} \times \vec{u} \tag{4.5}$$

The existence of vorticity generally indicates that viscous effects are important. This occurs because fluid particles can be set into rotation by an unbalanced shear stress.

The vorticity is directly proportional to the shear shear [14]. For simplicity we demonstrate this in 2D case, then we extend it to the 3D case.

As expressed in Equation 4.5, the vorticity components are:

$$\begin{cases} \vec{w_r} = \frac{1}{r}\frac{\partial u_z}{\partial \theta} - \frac{\partial u_\theta}{\partial z} \\ \vec{w_\theta} = \frac{\partial u_r}{\partial z} - \frac{\partial u_z}{\partial r} \\ \vec{w_z} = \frac{1}{r}\frac{\partial (r u_\theta)}{\partial r} - \frac{1}{r}\frac{\partial u_r}{\partial \theta} \end{cases} \tag{4.6}$$

The shear stress, for a Newtonian fluid, in a local frame system, in a section of the pipe, where z is the component of the velocity exiting from the section ard r parallelin, is given by:

$$\vec{\tau} = -\mu \frac{\partial u_z}{\partial r} \tag{4.7}$$

Since the velocity does not vary with θ we have that:

$$\begin{cases} \vec{w_r} = -\frac{\partial u_\theta}{\partial z} \\ \vec{w_\theta} = \frac{\partial u_z}{\partial r} \\ \vec{w_z} = \frac{1}{r}\frac{\partial (r u_\theta}{\partial r} \end{cases} \tag{4.8}$$

from this it follows that:

$$\vec{\tau} = -\mu \vec{w_\theta} \tag{4.9}$$

In a straight pipe, the vorticity is axisymmetric, and in particular is zero in the axis of the pipe and higher in the wall; while in a curve the vorticity is not axisymmetric, but the minimum moves to the outer bend, in agreement with the displacement of the maximum axial velocity, and its value in the outer wall is greater than the inner one as shown in Figure 4.8:

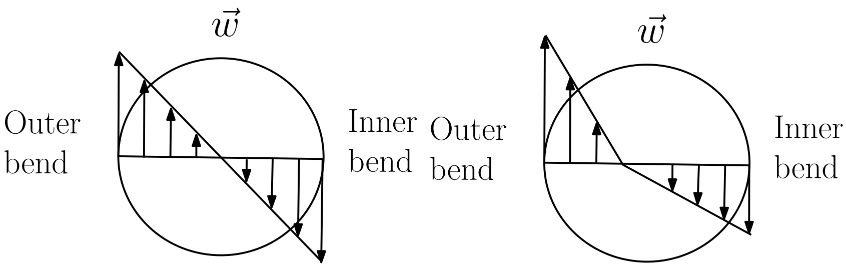

(a) a (b) b

Figure 4.8: The qualitative trend of the vorticity:(a) in a straight pipe; (b) in a curve pipe.

Through the use of Paraview we analyze behavior of vorticity in the geometry described in Section 4.1.2. Because the results of the simulation (obtained with lifev) are: velocity and pressure, the vorticity is calculated using the filter: “python calculator”, with which we calculate the curl of velocity. In the Figure 4.9 is portray the result of the vorticity as function of different bending angles.

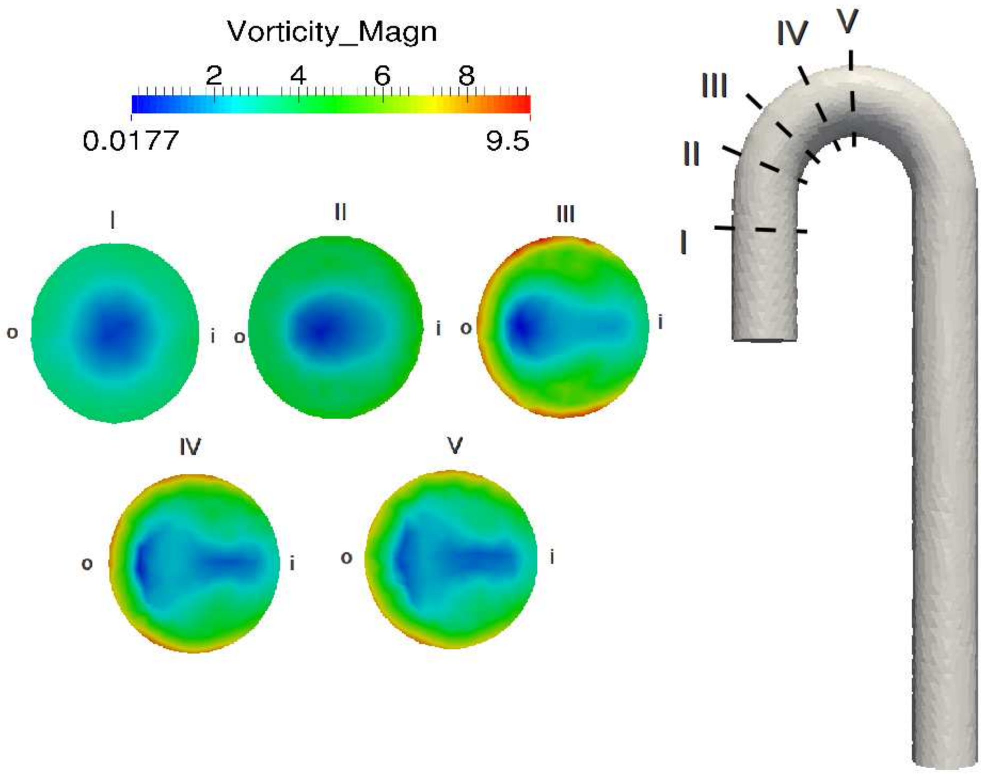

Figure 4.9: Qualitative trend of the vorticity $[s^{-1}]$, shown for several cross-section. The figure shows thst the minimum of the vorticity shifts towards the outer bend in the bend

At $\theta = 0$, the influence of the curvature is not visible, in fact, the vorticity is equal to that which is found in a straight pipe. To increase the angle of curvature, we can see that the minimum moves to the outer wall and that the vorticity is not longer axisymmetric, but its value becomes higher in the outer wall than in the inner one as shows in Figures 4.9, 4.10.

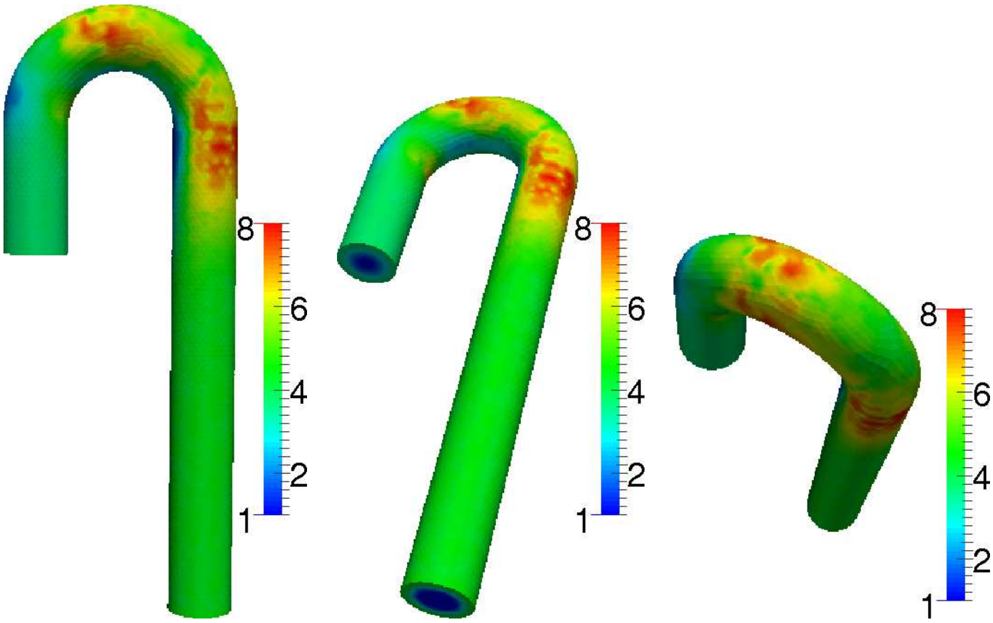

(a) Front view (b) View from above (c) View from below

Figure 4.10: Qualitative analysis of the distribution of values of vorticity $[s^{-1}]$ in a candy cane where is applied a steady inflow. The vorticity is shown in three different views: front, from below and from above. The picture shows that the maximum values of vorticity are in the outer wall of the pipe.

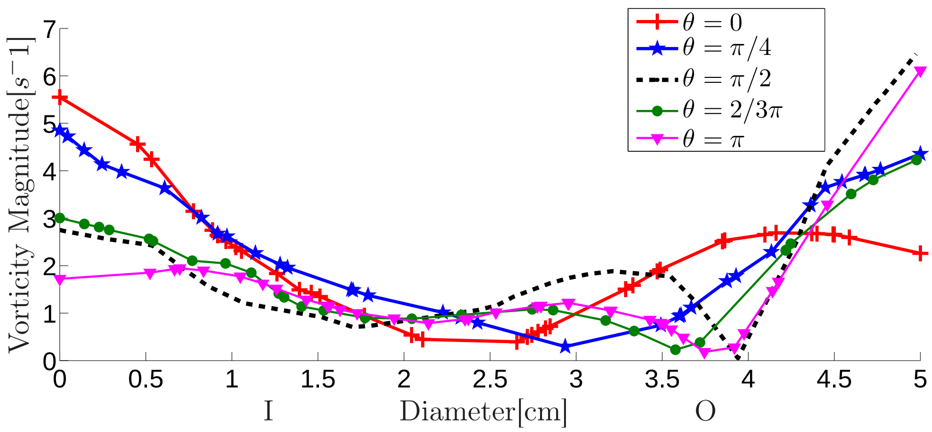

Figure 4.11: Analysis of the vorticity, in the plane of symmetry of the curved tube, for different bending angles. The graph shows that the greater the angle of curvature, the more the minimum of the vorticity is shifted towards the outer bend and its value becomes higher in the outer wall than the in the inner one . O,I denote outer and inner bend, respectively.

4.2.3 Wall shear stress

Any real fluids moving along solid boundary will incur a shear stress on that boundary. The no-slip condition dictates that the velocity of the fluid at the boundary must be zero, but at some height from the boundary the flow velocity must equal that of the fluid. For all

θ	w_i	w_o
0	0.196	0.199
$\pi/4$	0.162	0.349
$\pi/2$	0.155	0.543
$2/3\pi$	0.174	0.294
π	0.045	0.435

Table 4.2: Analysis of the wall shear stress at the different bending angles $\theta = 0; \pi/4; \pi/2; 2/3\pi; \pi$. The values are expressed in $[dyne/cm^2]$

Newtonian fluids in laminar flow the shear stress is proportional to the strain rate in the fluid where the viscosity is the constant of proportionality.

The shear stress, for a Newtonian fluid, in a local frame system, in a section of the pipe, where z is the component of the velocity exiting from the section ard r parallelin, is given by:

$$\vec{\tau} = -\mu \frac{\partial \vec{u}}{\partial r} = \mu \vec{w}_\theta \tag{4.10}$$

The negative sign is included to give > 0 with $\partial \vec{u}/\partial r < 0$, because the velocity decreases from the pipe centerline to the pipe wall.

The wall shear stress,, is defined as:

$$\vec{\tau} = -\mu \frac{\partial \vec{u_z}}{\partial r} = \mu \vec{w}_\theta |_{r=R} \tag{4.11}$$

To calculate the wss in curved pipes, we use a routine of Lifev. We analyze the trend of the wss according to the angle of curvature. To do this we derive the data for the section $\theta = 0; \pi/4; \pi/2; 2/3\pi; \pi$; by the filters “slides” and “plot on intersection curved”, then and process it by Matlab.

At $\theta = 0$ the values of wss are similar; while in the bend its value in the outer wall is greater than the inner one as shows in Figure 4.12.

4.2.4 Axial velocity VS Dean number

Another important dimensionless parameter, that we have already introduced in Section 4.1.2, is the curvature ratio, expressed in the equation 4.3 In this section we study what happens to vary R_c .

We built three geometries (CSG method) that differ only by the radius of curvature and realize the computational grid by Netgen.

In the table we summarize the characteristics of the computational domains: After running the simulations for the three geometries, we extract the data relating to the velocity and

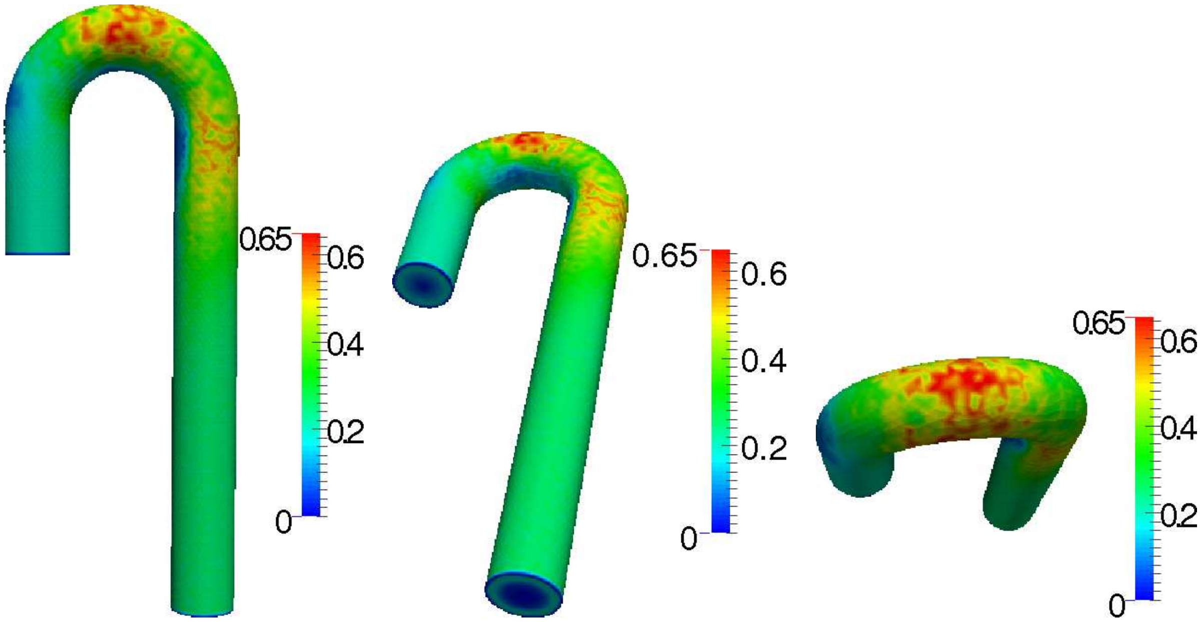

(a) Front view (b) View from above (c) View from below

Figure 4.12: Qualitative analysis of the distribution of values of wss $[dyne/cm^2]$ in a candy cane where is applied a steady inflow. The vorticity is shown in three different views: front, from below and from above. The picture shows that the maximum values of wss are in the outer wall of the pipe.

case	D	Rc	δ	$\vec{u}$	Re	De	elements mesh
1	5 cm	3.5 cm	1.42	2.5 cm/s	$\cong 335$	$\cong 280$	61672
2	5 cm	6.5 cm	0.77	2.5 cm/s	$\cong 335$	$\cong 200$	66992
3	5 cm	13 cm	0.38	2.5 cm/s	$\cong 335$	$\cong 140$	77680

Table 4.3: Characteristics of the computational domains

vorticity for different angles of curvature ($\theta = 0; \pi/4; \pi/2; 2/3\pi; \pi$), through Paraview and we analyze them with Matlab. In the graphic 4.13 is reported only the results of the section $\theta = \pi$. In the Section 4.2, we showed that at the increase of the degree of curvature the maximum axial velocity moves more and more towards the outside of the curvature and its maximum decreases;because $\theta = \pi$ is near the exit of the curve, we expect that here the effects of curvature on the velocity and/or vorticity are more evident than in the section near the entry; We analyze the trend of the velocity or vorticity as a function of the diameter for different radii of curvature.

The analysis was conducted in geometries that differ only for the radius of curvature, in which the same fluid flowing at the same velocity.

The Figure 4.13 makes known that for R_c the maximum of the axial velocity is in corre-

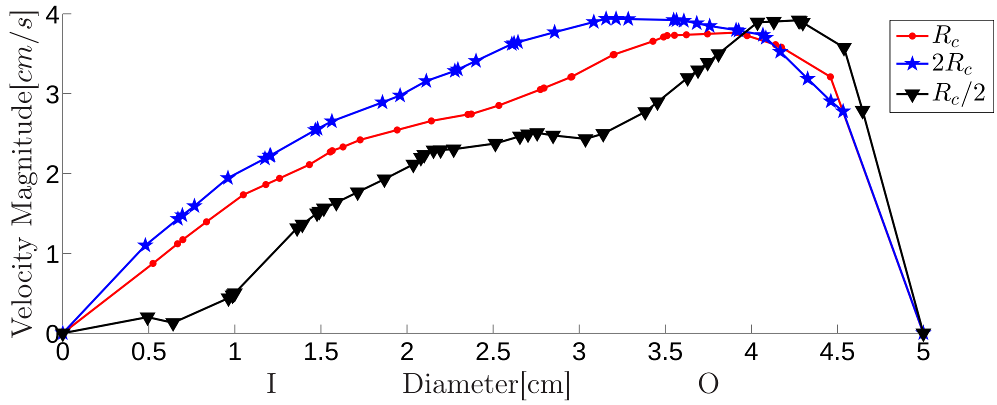

Figure 4.13: Analysis of the axial velocity at different R_c for $\theta = \pi$. The graph shows that at the decrease of R_c the maximum of the axial velocity is more shifted.

spondence of $d \cong 3.6$ cm. For $R_c/2$ we observe that the maximum of the velocity is for $d \cong 4.3$ cm, then is more shifted outwards with respect to the previous case. Instead to $2R_c$ the maximum is for $d \cong 3.2$ cm, then it is more centered than in the case ofR_c and $R_c/2$. Generalizing we deduce that to decrease of the radius of curvature, the maximum axial velocity is more shifted towards the outside of the curvature; this is explainable because the centrifugal force is inversely proportional to the radius of curvature; consequently the fluid in the geometry with smaller radius of curvature will undergo a greater centrifugal force.

A similar argument can be made for the vorticity and for the wss.

In the graph in Figure 4.14 we observe that for the radii of curvature smaller, the minimum value of the vorticity is more shifted towards the outside of the curvature In fact the Figure

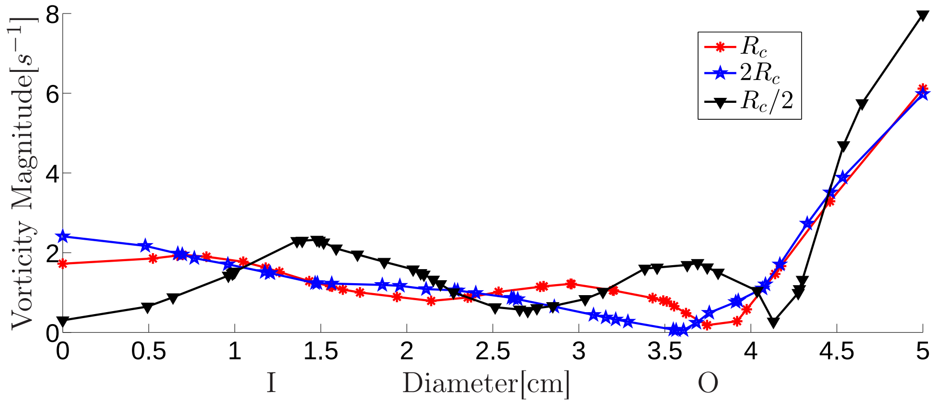

Figure 4.14: Analysis of the vorticity at different R_c for $\theta = \pi$. The graph shows that at the decrease of R_c the minimum of the vorticity is more shifted.

4.14 evidence that for R_c the minimum of the vorticity is in correspondence of $d \cong 3.6$ cm; while for $R_c/2$ the vorticity is for $d \cong 4.3$ cm, then is more shifted outwards with respect to the previous case. Instead to $2R_c$ the minimum is for $d \cong 3.2$.

case	w_i	w_o
$R_c/2$	1.14 cPa	5.078 cPa
R_c	0.453 cPa	4.354 cPa
$2R_c$	0.951 cPa	2.3 cPa

Table 4.4: Analysis of the wss at different R_c for $\theta = \pi$. The table shows that at the decrease of R_c the values for both wss w_i that for w_o decrease. Where w_i is the inner wall and w_o the outer one .

In the Table 4.4 we observe that for $R_c/2$, in the outer bend the wss assumes the value greater than the other two cases and in the inner bend the lower value. R_c has the opposite behavior. We deduce that to decrease of the radius of curvature, increase the value of wss at outside of the curvature, while decrease its value at inside of curvature.

4.2.5 A Vorticity Qualitative Index

To be able to compare the vorticity to the vorticity found in other experiments, it is made dimensioneless by:

$$\vec{w}' = \frac{L}{V}\vec{w} \tag{4.12}$$

where L in the characteristic length and V the characteristic velocity. To quantify the vorticity, through paraview, we selected a subset of nodes of the computational domain and for their we extracted data relating to the vorticity. Matlab is used to compute the dimensioneless average vorticity introduced in Equation 4.13 by summing the absolute values of the vorticity in the nodes and dividing by the number of nodes:

$$\vec{w}' = \frac{1}{N}||\vec{w}'|| \tag{4.13}$$

in which N is the number of nodes selected.

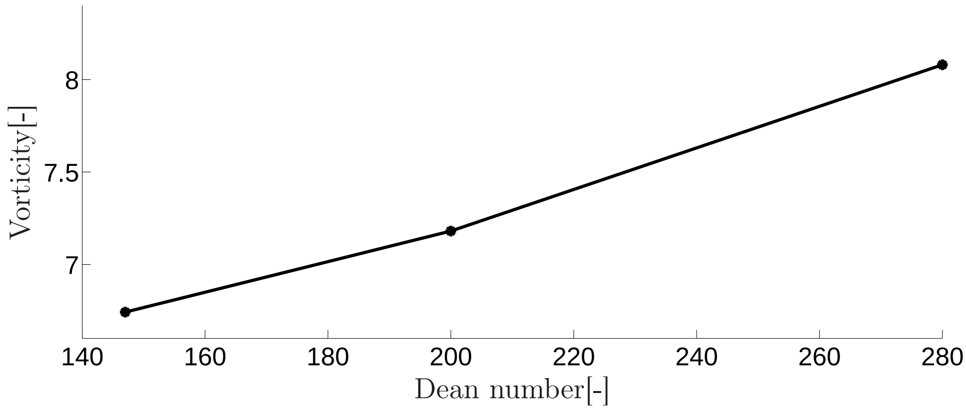

Figure 4.15: Analysis of vorticity with the increase in the number of Dean number for different radii of curvature. As the number of Dean increases the vorticity increases too.

In the Figure 4.15, vorticity $\vec{w}'$ is plotted as a function of the Dean number. We can see that as the number of Dean increases the vorticity increases too.

4.3 Unsteady flow in a curved pipe

Studying flow in curved tubes with unsteady entry flow is more interest in physiological flows since in the aorta the flow is periodic and pulsatile.

There are several studies that deal with unsteady flow in bends. Among them, particularly interesting is the article by Lyne [11].

Lyne has presented analysis of oscillatory flow in curved tubes.

As reported in the chapter 5 of the book [3], Lyne describes that the secondary flow generated by the centrifugal forces are confined to the thin Stokes layer. The fluid in this boundary layer moves from the outer wall toward the inner wall along the wall and returns to the outer wall at the edge of the boundary layer. The boundary layer secondary flow drags the fluid in the core region with it resulting in a secondary flow in the core region in the opposite direction. Hence in oscillatory flow along a curved tube, the axial velocity profiles are skewed toward the inner wall of the curve.

This leads us to say that in the case of unsteady inflow, results very likely will be different from those obtained in the case of steady inflow.

In this study, we create a candy cane that has dimensions closer to those of the aorta, in particular, we choose the diameter of the candy cane equal to 3.3 cm and the radius of curvature of about 10 cm. At the inlet, a flat and parabolic flow velocity profile is used together with a pulsatile waveform, as show in Figure 4.18, based on literature data. The results will be analyzed only in the case where the velocity profile is parabolic, because, as

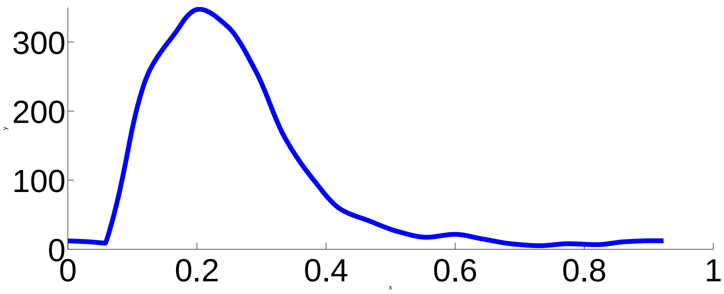

Figure 4.16: Candy cane inlet velocity pulse shape.

shown in the Figure 4.17, the axial velocity has the same behavior in the two cases. The only difference is in the first part of the candy cane, because in the case of a parabolic profile, at the entry, is imposed directly the parabolic solution, while in the other case the solution is to be developed.

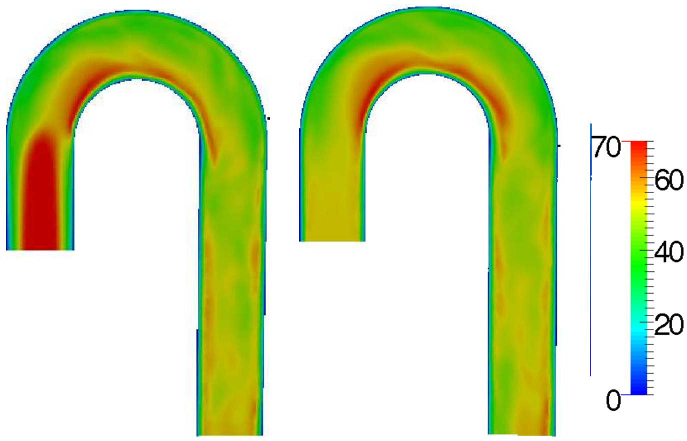

(a) Parabolic profile (b) Flat profile (c) Velocity scale

Figure 4.17: Qualitative analysis of the distribution of values of axial velocity [cm/s] in a candy cane where is applied an unsteady inflow. On the left, the velocity profile is showed for a parabolic shape profile. On the right, the velocity profile is showed for a flat shape profile. The picture shows that in both cases the speed has the same behavior in the curvature.

4.3.1 Axial velocity

The results in the figure show that the trend of the axial velocity is different compared to the case in which we apply a steady flow at inlet. As in the previous case, we analyze the axial velocity in the cross section. The candy cane begins with a straight pipe, here we find the results of Poiseuille and the velocity remains undisturbed, i.e unidirectional, until the bend. At the beginning of the curvature, the axial velocity is skewed toward the inner wall of the tube until the end of the curvature, at the end of the bend we have another straight section where again we find the condition of Poisuille. As written before Lyne said that the secondary

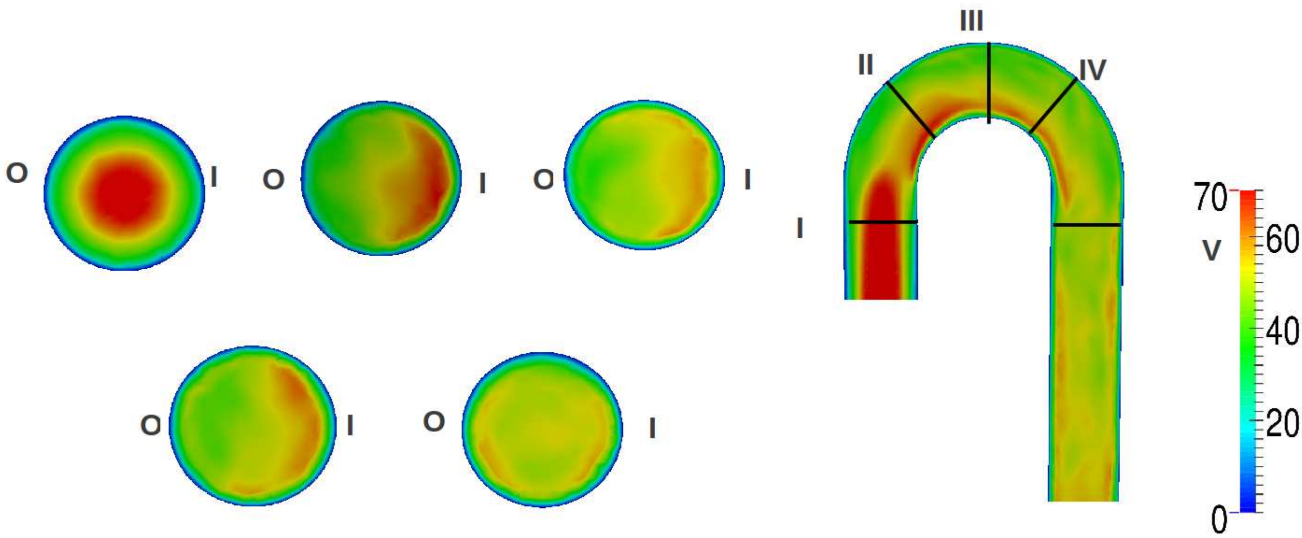

Figure 4.18: Qualitative trend of axial velocity, shown for several cross-section at the peak of the inflow. The axial velocity is skewed toward the inner wall of the curve

flows are confined in a thin boundary layer. This could justify the fact that in our analysis we are not able to display secondary flows.

4.3.2 Vorticity

In section 4.2.2 we have seen that in the case of curved pipe, where is applied a steady inflow, the minimum of the vorticity moves towards the outside of the curvature and the maximum values are in the outer wall of the tube, in agreement with the results of the axial velocity. In the present case the minimum of the vorticity moves towards the inside of the curvature and the maximum values of vorticity are in the inner wall of the curvature, according to the trend of the axial velocity, as shown in the Figure 4.19.

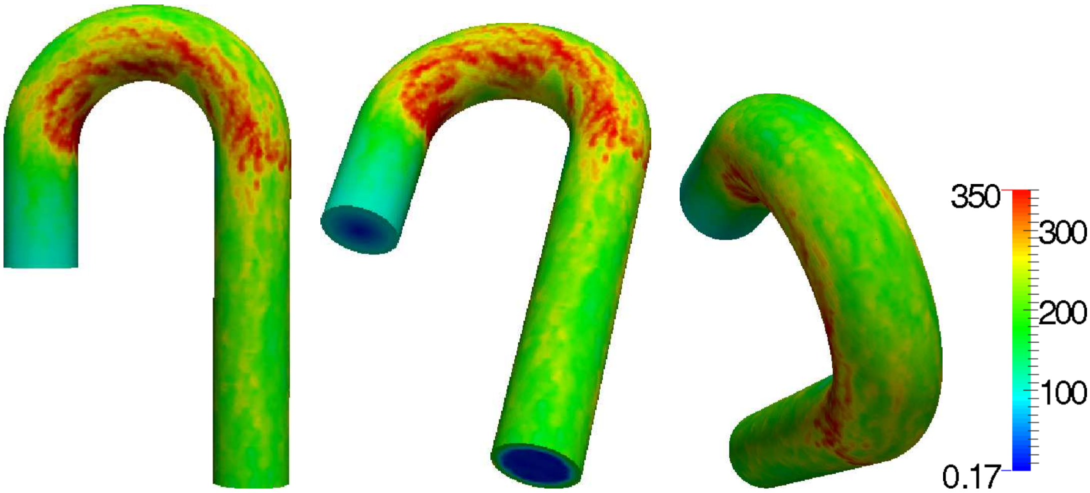

(a) Front view (b) View from above (c) View from below (d) wss scale

Figure 4.19: Qualitative analysis of the distribution of values of vorticity $[s^{-1}]$ in a candy cane where is applied an unsteady inflow. The vorticity is shown in three different views: front, from below and from above. The picture shows that the maximum values of vorticity are in the inner wall of the pipe.

4.3.3 Wall shear stress

Even in the case of wss, there are substantial differences between the previously studied case and the present one. As shown in the Figure 4.20, in this case the maximum values of wssare in the inner wall instead of the outer wall, in accordance with the values of vorticity found in the Section 4.3.2.

These outcomes are in agreement with those found by Chandran [4], summarized in the article [3], which shows that Chandram Chandran et al. have analyzed the flow development of pulsatile flow (unsteady flow with nonzero mean) in curved tubes. A pulsatile pressure trace was decomposed into the steady and first six oscillatory flow components in simulating the physiological pulsatile flow. Their results showed that the wall shear stresses for the steady flow component resulted in higher magnitudes along the outer wall of curvature. However, superposition of the first six oscillatory component on the steady flow component resulted in wall shear stresses an order of magnitude higher than the steady flow magnitudes with higher magnitudes along the inner wall of curvature.

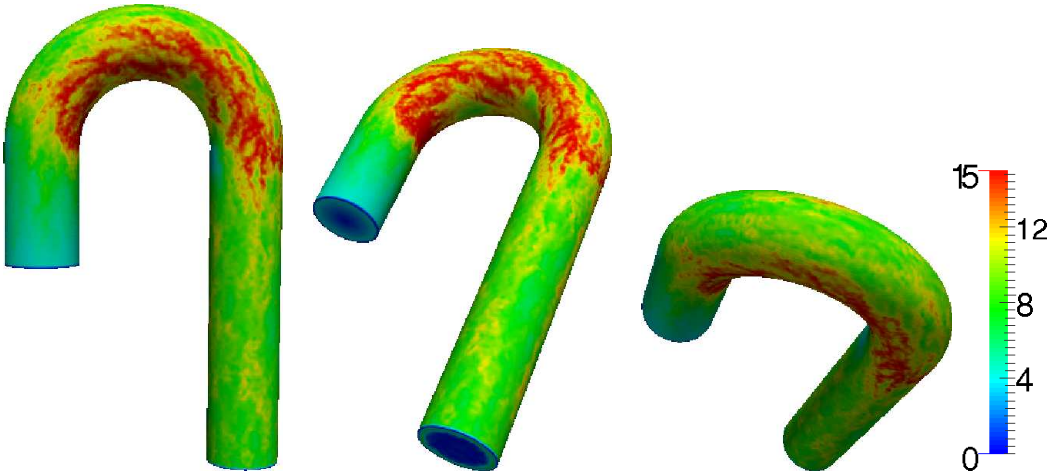

(a) Front view (b) View from above (c) View from below (d) wss scale

Figure 4.20: Qualitative analysis of the distribution of values of wall shear stress $[dyne/cm^2]$ in a candy cane where is applied an unsteady inflow. The tren of wss is shown in three different views: front, from below and from above. The picture shows that the maximum values of wall shear stress are in the inner wall of the pipe.

Chapter 5

Study Of The Blood Flow In Healthy Aorta

The cardiovascular system is an internal flow loop with curves and multiple branches in which a complex liquid circulates.

The first phase of the cardiac cycle is the ventricular **diastole** that happens when the ventricles are relaxed and allow for the newly oxygenated blood to flow in from the atria. Ventricular diastole is followed by systole, where the ventricles contract and eject the blood out to the body, through the aorta. Aortic pressure rises when the ventricles contract, pumping the blood into the aorta, and, at its maximum is termed **systolic** pressure. At the start of following cardiac cycle, as the blood begins to flow into the ventricles, the aortic pressure is at its lowest, and it is known as diastolic pressure.

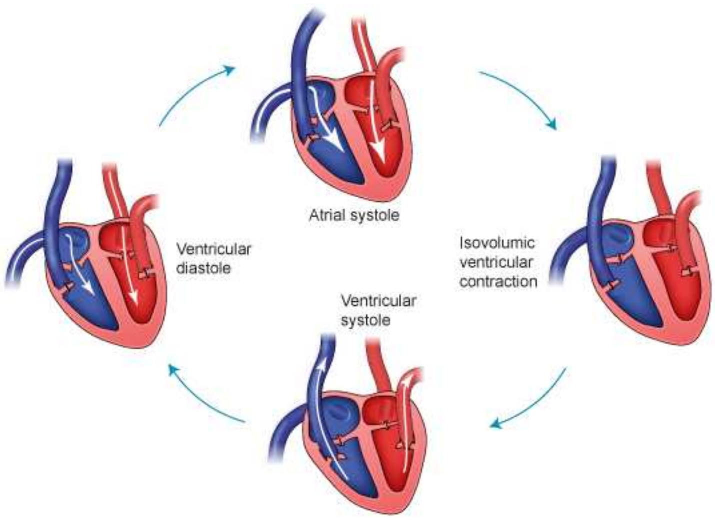

Figure 5.1: Cardiac cycle phases

The cardiovascular system primarily functions in nutrient and waste transport throughout the body.

Laminar flow is the normal condition for blood flow throughout most of the circulatory system, with secondary flows generated at curves and branches. In certain circumstances may develop unusual hemodynamic conditions, characterized by decrease of the flow, and departs from unidirectionals patterns (in fact vortices are formed); that can create an abnormal biological response [10]. Altered velocity profile can lead to changes of the forces acting on the vessels' walls (wall shear stress); that are capable of stimulating the endothelium to produce several cellular factors that can inhibit or promote inflammatory events [20]. In particular low and oscillating wall stresses contribute to atherosclerotic plaque growth by activating both mechanical and biological pathways [2], that narrows the artery lumen. Indeed too high shear stress may induce initial endothelial lesions, which in turn activates inflammatory response with possible platelet aggregation and stenosis takes place.Stenosis can cause turbulence and reduce flow and if it is acute can totally block blood flow to the heart or brain.

Blood flow under normal physiologic conditions is an important field of study, as is blood flow under disease conditions since the local flow behavior of blood is certainly implicated in the formation of atherosclerotic plaques and of phenomena such as thrombogenesis, atherogenesis, endothelial damage, intimal thickening and hyperplasia.

The purpose of this study is quantitatively evaluate the hemodynamics of a healthy aorta, with the aim to create a reference model that can later be used to determine how much a pathological case deviates from normal condition.

5.1 Anatomical Overview

The aorta is the largest blood vessel in the human circulation, arises from the left ventricle, from which it receives blood during the contraction of the heart, and extending down to the abdomen, where it bifurcates into two smaller arteries (the common iliac arteries)(Figure 5.2). The blood from the aorta flows to the visceral organs and to the peripheral regions in the systemic circulation.

The aorta has a complex, three-dimensional curved geometry with multiplanar curvature. As shown in Figures 5.2 and 5.3, the aorta begins at the aortic valve and makes its first bend, past the pulmonary vessels and bronchi. A second curvature allows it to bypass the esophagus and the trachea. In the end the last plane of curvature allows it to bend around to the left atrium.

As shown in the Figure 5.2, the aorta divides into:

- **The ascending aorta** is the initial portion of the aorta. It has its origin at the level

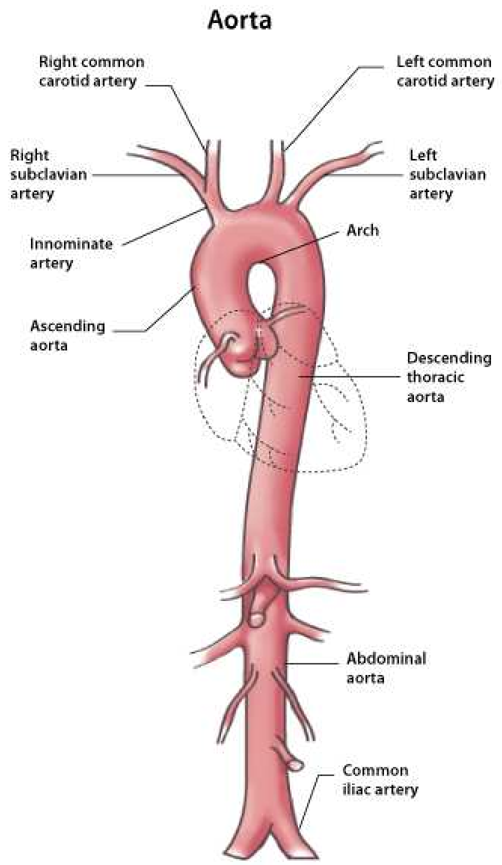

Figure 5.2: Aorta Anatomy.

of the aortic valve. It runs obliquely, upward and to the right, until it reaches the edge of the second costal cartilage, where it ends by continuing in the aortic arch.

- **The aortic arch** follows the ascending aorta at the level of the second costal cartilage. It moves back, to the left, to reach the left margin of the body of the fourth thoracic vertebra where it continuing with the descending aorta.

  From aortic arch originate the brachiocephalic trunk (innominate artery), which divides into the right subclavian and right carotid artery, the left carotid and the left subclavian artery, which carry blood to the head, neck and shoulders.

- **The descending aorta** is the last section of the aorta. It is composed of two sections: thoracic aorta and abdominal aorta.

The cross-section of the aorta is approximately elliptical, with the lumen diameter being slightly larger in the anterior–posterior plane compared to that in the lateral plane.

We will consider only the upper portion aortic arch.

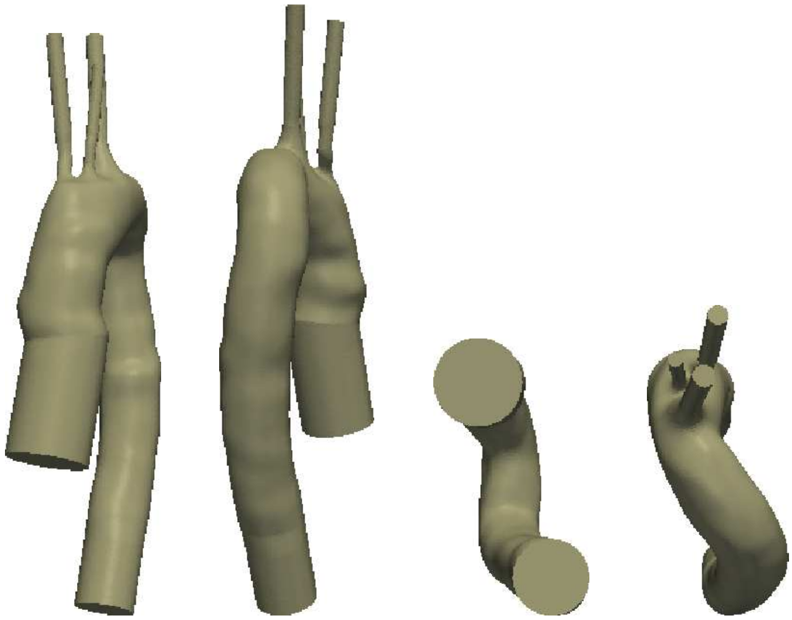

(a) Front view (b) Front from behind (c) View from above (d) View from below

Figure 5.3: Representation of the aorta showing the different planes of curvature of the aorta

5.2 From Clinical Image To Computational Domain

The advent of high resolution image system acquisition allows to obtain information about the vivo anatomy of blood vessel in a non invasive way. By employing this information as the domain definition for computational fluid dynamics, it is possible to model hemodynamics in realistic geometric configurations on a subject-specific basis [17]. Since geometry has a strong influence on hemodynamics, the procedure used to model the geometry of a blood vessel from medical images plays a primary role in determining the reliability of hemodynamic predictions and, ultimately, their clinical significance.

In the following we illustrated the adopted work flow, highlight how we generate the computational domain from medial images regarding the specific clinical case under investigations. Once the geometric model of the vessel of interest is created,it is discretized into a grid, suitable for numerical simulation.

The process from images to computational meshes to represent realistic vascular geometries involves several separate steps shows in the Figure 5.4 Sets of images are first acquired using one of the clinically available imaging techniques. The most used techniques in the clinical practice, to produce 3D patient-specific representations are: CT(Computer Tomography) and MRI(Magnetic Resonance Image). We will use images from CT, with contrast medium. The CT is an imaging technique that captures images by detecting the attenuation that ionizing

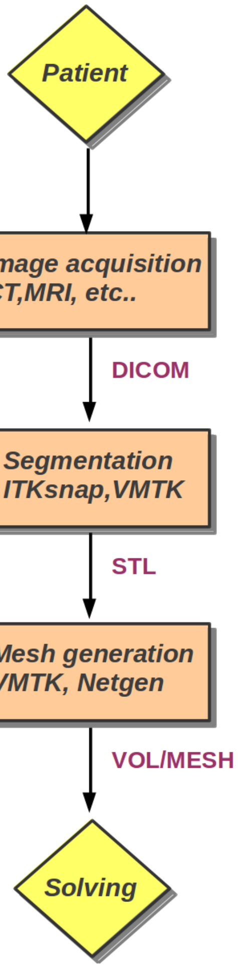

Figure 5.4: Flow chart:from patient to computational$_domain$

radiation undergo when they pass through body tissues. The level of attenuation depends on the absorption capacity of the tissues. In the procedure of acquisition of CT image, the patient is hit by a beam of ionizing radiation at different angles, for each angle, in the opposite part of the source detector is capable of collecting attenuation data that radiation undergo in their path within the organization. The measured data are organized in a matrix called sinogram and processed through a process called reconstruction tomography approx. Thus we get the image that represents the information of attenuation expressed in HU (Hounseld unit) and displayed using a gray scale (Figure 5.5), according to which the darker values characterize tissues and areas of low density, namely low attenuation as the air and most of the biological soft tissues, while lighter values characterize high density tissues such as bone or areas with the presence of calcium. The image is is organized into cross-sections according to the three anatomical planes (sagittal, frontal and medial) and it is displayed slide by slice The use of images, obtained with the CT, for the study of the patient-specific hemodynamics,is possible

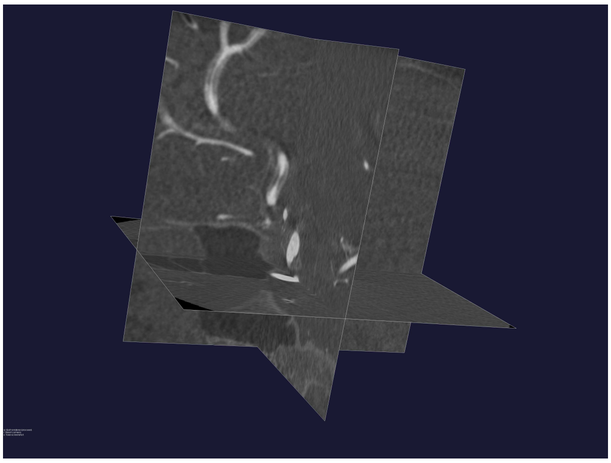

Figure 5.5: Dicom series open with VMTK

only after their processing, which allows to obtain a calculation grid.

In this case, we investigate a real clinical case. We will perform computational fluid dynamics (CFD) analysis on patient-specific vasular model derived from medical image, which has been captured by CT with contrast medium.

To extract the computational domain from the series dicom, obtained by CT, we will use itksnap; while to generate the mesh we will use VMTK, (which was introduced in the Section 3.1.1)

5.2.1 Segmentation

Segmentation is the extraction of an area of interest from an image volume. The segmentation result is the computational domain of numerical simulations, so it assumes a key role. Incorrect segmentation can lead to a simulation meaningless. We do the segmentation by the open-source software **ITK-SNAP**.

ITK-SNAP is a software application used to segment structures in 3D medical images. It provides a set of tools to make segmentation of volumetric data easier and faster. It can be used in two different modes: manual segmentation and semi-automatic segmentation. First we will use the semi automatic method, which allows us to obtain a coarse segmentation and to clean up the this results, we will use the manual mode.

The input of this program is a dicom series, that are organized into cross-sections according to the three anatomical planes: Sagittal, Frontal and Axial; and it is visualized in gray scale, slice by slice.

Once the data is loaded, we get the image of the whole volume that represents the information of attenuation expressed in HU (Hounsfield units); since the soft tissues have low attenuation, for the reconstruction of the vessel geometry, a fundamental role is played by the blood. Blood is a low attenuation tissue, therefore the CT technique, see before, are performed by injecting, within blood flow, a contrast medium, i.e a substance with an high absorption index, in this way blood attenuation will be as high as the bone tissue. This allow us to recognize and to close off (during the segmentation) the vessel to the other soft tissue.

Now we have to select the region of interest. The 3D segmentation algorithm used a threshold technique to determine the edges of the vessels. Once an adequate threshold is set, 3D bubbles approximately the diameter of the vessel are placed throughout the vessel to be segmented. Bubbles placed within the axially reconstructed images produced the models that most accurately replicated the anatomy of the vessel. Once the vessel is sufficiently filled with bubbles, expansion and contraction forces are set to limit the expansion of the bubbles and ensure they remain mostly within the vessel. In some cases, the progression passes out of the vessel lumen and these regions needed to be cut away. These regions can be selected and eliminated inTKSnap. The resulted model is stored in **stereolithography representation (STL format)**, depicted in Figure[5.6]:

Figure 5.6: Segmentation result

Now we illustrate how to process the surface model obtained in the Section[5.2.1] ,to generate a computational mesh for use in CFD. We have a 3D surface model of a vascular segment with blobby closed ends.

5.2.2 Smoothing

Image segmentation can result in bumpy surfaces, especially if the image quality is not high and one didn't use any curvature term in level sets evolution. Since bumps in the surface can result in spurious flow features and affect wall shear stress distributions, one may want to increase surface smoothness prior to building the mesh. The instruction that allows it is: **vmtksurfacesmoothing**.

5.2.3 Clipping

If we generated a surface using a deformable model, the surface could be closed at inlets and outlets. We will now proceed opening the surface by interactive command **vmtksurfaceclipper**. It allows us to choose manually the parts to be cut like in Figure 5.7 .

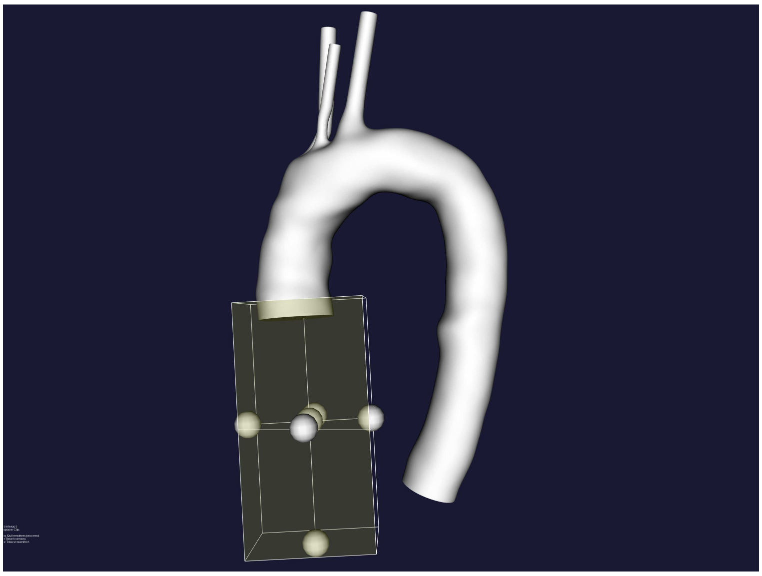

Figure 5.7: Open Surface

5.2.4 Adding Flow Extensions

Flow extensions are cylindrical extensions added to the inlets and outlets of a model. They are important to ensure that the flow entering and leaving the computational domain is fully developed. To achieve the extensions, we use the command **vmtkflowextensions** we add the extensions to the initial domain;

Figure 5.8: Flow extensions

5.2.5 Generating A Mesh

To generate a mesh suitable for CFD from a surface, we use the command **vmtkmeshgenerator**. This command is characterized by the flag **-edgelength**, that defines the absolute nominal length of a surface triangle edge and it allows to obtain calculation grids more or less fine. We set edgelength to 0.1; in this way we obtain a mesh consisting of 3415116 elements depicted in Figure 5.9. We use tetrahedral elements, which are particularly versatile and suited for complex geometries like the considered one.

5.3 Numerical Model and simulation process

Numerical simulations is carried out by solving the incompressible unsteady Navier-Stokes equations in the region on interest, i.e the lumen of the aorta. The goal is to obtain a characterization of bloodflow parameters (velocity and pressures).

The Navier-stokes equations for an imcompressible, continuum and Newtonian fluid were extensively discussed in Section [2.1] and for simplicity they are reprint below in Equation [5.1].

$$\begin{cases} \dfrac{\partial \vec{u}}{\partial t} + (\vec{u} \cdot \nabla \vec{u}) = -\dfrac{\nabla p}{\rho} + \nu \nabla^2 \vec{u} + \vec{f} \quad \text{on } D \subset \Omega \subset; \quad 0 < t \leq T \\ \nabla \cdot \vec{u} = 0 \quad \text{on } D \in \Omega \end{cases} \tag{5.1}$$

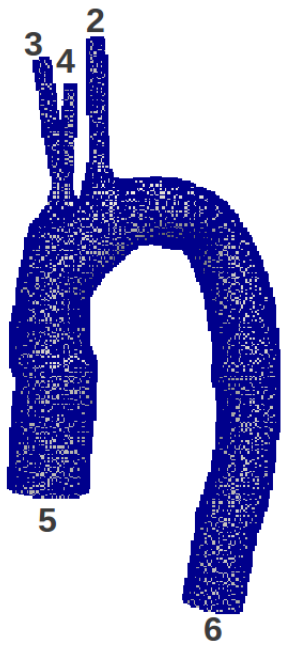

Figure 5.9: Image of the mesh with the label of the label of the boundary conditions realized by VMTK

where Ω is the lumen of the aorta and T is the duration of the time interval of interest. The term f represents the possible action of the external forces, and is often taken equal to zero in hemodynamics.

The vessel wall will considered to be rigid

The Equations [5.1] need to be completed by suitable initial and boundary conditions on $\partial\Omega$. The choice of boundary conditions is a very important task, in fact by choosing suitable boundary conditions on inflow and outflows, it is possible to achieve physiological relevant distributions of velocity and pressure in the computational model.

5.3.1 Initial condition

The initial condition represents, in this case, the initial status of the fluid velocity $u_0(x)$ con $x \in \Omega$. It can not take arbitrary, but it has to satisfy the conservation equation $\nabla \cdot \vec{u_0} = 0$. As suggested in the Book [Quarteroni], we adopt null velocity.

5.3.2 Boundary conditions

As boundary conditions, for our domain, we distinguish three types of boundaries (referring to Figure 5.11):

- wall Γ_w
- inlet Γ_{in}
- outlets Γ_{out}

The artery wall Γ_w in this work is modeled as rigid, with a no-slip boundary condition (i.e. fluid velocity at the wall is zero). This assumption can influence the result, because a real artery is distensible; in fact aortic diameter can under certain circumstances change in the range of 10%, during a cardiac cycle. One reason of the rigid wall boundary condition assumption is that the numerical simulation that including wall movement is very complex.

On the arterial wall we prescribe zero velocity.

Inlet and outlets boundaries are often indicated as artificial boundaries since they do not correspond a physical interface between the fluid and the exterior, but sections that have been artificially created to separate the region of interest for our investigation from the remaining part of the circulatory system. The set up of boundary conditions on artificial boundaries is an important issue for fluid dynamic computations.

In particular the inflow boundary condition is set here, in terms of flow rate, with flat profiles. The flow rate is assigned using data from literature, because the experimental data are not available. The flow that, we have chosen is laminar, it is characterized by flat inflow velocity for the axial velocity and zero transverse velocity component.

For the outflow boundaries, i.e at the ends of the branches and the distal end of the aorta, a powerful and versatile solution consists of coupling the model with a one-dimensional model of flow, which simplifies the entire cardiovascular system downstream boundaries. We adopt a three-element Windkessel lumped parameter model (rendered if Figure 5.10), designed in the late 1800's by the german physiologist Otto Frank, that represents with two resistances R_p, R_d and one compliance C of the distal circulation that are not physically included in the 3D geometrical model. The Windkessel model describes the cardiovascular system in terms of a

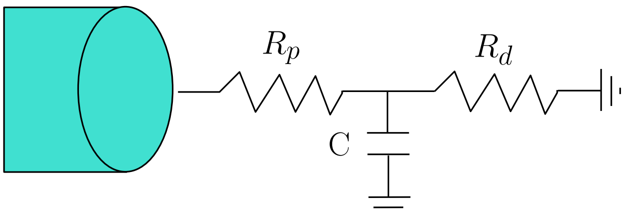

Figure 5.10: Outlets coupled to 3-element Windkessel models

compliant section in series with a resistive section. During systole, the compliant aorta acts like a capacitor to store blood. During diastole, the elastic aorta discharges the stored blood through the resistive branches of the smaller arteries to various organs. The pressure and flow waveforms given by this model are quite close to those measured in the body.

This approach presents important conceptual advantages:

- Kim showed how the velocity and pressure fields of the same computational domain can change significantly depending on the choice of outflow boundary conditions. Using this model, we do not rely on the specification of any of the primary blood flow variables (flow or pressure), which are generally not known and are part of the desired solution.
- The pressure and flow waveforms given by this model are quite close to those measured in the body.

The specific values of those parameters are taken from The Article [9] and we list them in the Figure below.

4 Common carotid artery	
R_p	1180
C	7.70E-5
R_d	18400

3 Brachicephalic artery	
R_p	1040
C	8.74E-5
R_d	16300

2 Left subclavian artery	
R_p	970
C	9.3E-5
R_d	15200

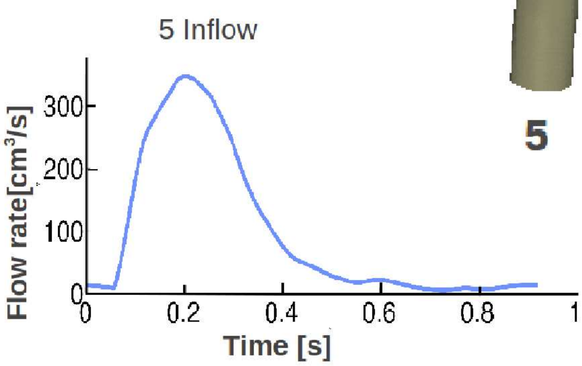

3 Descending thoracic aorta	
R_p	188
C	4.82E-4
R_d	2950

Figure 5.11: Specification of boundary conditions, for simulations of blood flow in a normal aorta

5.4 Results

To elucidate the possible connection between blood flow and localized pathogenesis and the development of atherosclerosis in humans, we studied the flow patterns and the distribution of fluid axial velocity and wall shear stress in the aortic arch in detail. The simulation is performed using Lifev, as explained in Appendix A. The problem is solved over four hearts beat to be sure that the initial condition and the boundary conditions do not influence the results; because, as an initial condition we set: $u_0(x) = 0 \quad \forall x \in \Omega$, it means that at each point of the domain, at time t=0, the velocity is zero. In the real case is not so, the initial velocity of a heart cycle corresponds to the final one of the previous cycle. In the simulation the velocity starts from zero and must reach the regime to simulate physiological conditions. Also the elements of the Windkessel model, starting from the initial values,found in literature, must change to adapt to the analyzed case.

As a trade-off between accuracy and computational cost, we use mixed P1Bubble/P1 elements, providing piecewise continuous linear interpolation enriched by a cubic bubble for velocities and piecewise continuous linear approximation for pressures.

Simulation is carried out on Dell R815, using 48 cores.

The analysis are performed using **Paraview**.

When analyzing the numerical results, we focus our attention on certain relevant time instants of the cardiac cycle. We select three times instants, expressed as a function of the cardiac cycle, shown in Figure [5.12]:

- $T_1 = 0.1T$, that represents the point of maximum acceleration of the blood flow;
- $T_2 = 0.2T$, that corresponds to the systolic peak;
- $T_3 = 0.3T$, that is the point of maximum acceleration of the blood flow.

5.4.1 Axial velocity Distribution

A very important aspect of the analysis of three-dimensional flows in the aorta is the graphical presentation of the flow field. In the Figure 5.13 we represent the axial flow velocity in the aortic arch at T_1 , T_2, T_3. To simplify the analysis, we exclude branches: the brachiocephalic trunk, the left carotid and the left subclavian artery, to focus our attention to the effects of curvature.

The next analysis will be conducted at the systolic peak. This choice is motivated by the results in Figure 5.13, where we evince that the behavior of the axial velocity in the three times is qualitatively very similar, but the order of magnitude changes. Furthermore, this choice is

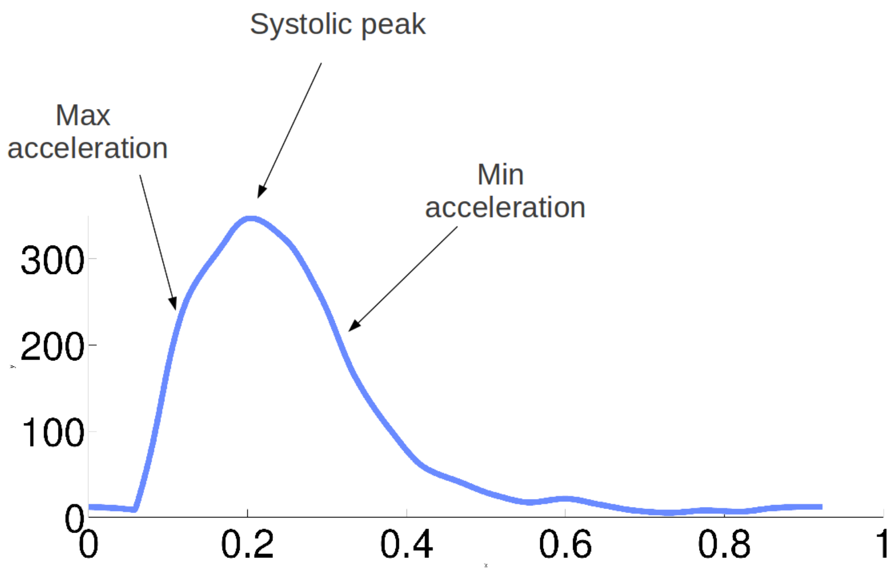

Figure 5.12: Aorta inlet flow shape

supported by the results of the article by N. Shahcheraghi [15]. He qualitatively shows that the flow has approximately the same trend over time. This velocity profile is induced by the

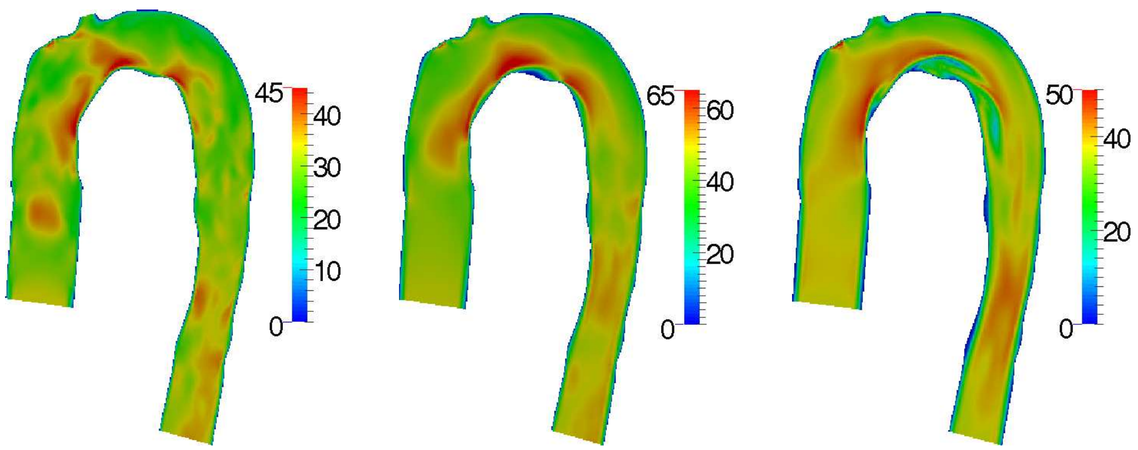

(a) T_1 (b) T_2 (c) T_3

Figure 5.13: Analysis of the axial velocity of blood flow in the aortic arch to the three times: $T_1 = 0.1T$, $T_2 = 0.2T$, $T_3 = 0.3T$. To simplify the analysis, we exclude the branches, to focus only on the aortic arch. The behavior of the axial velocity in the three times is qualitatively very similar, what changes are orders of magnitude. The figure shows that the axial velocity is skewed toward the inner wall of the curve

unsteady inflow, as we prove applying the same unsteady inflow that we applied at the inlet of the aorta, to the candy cane as shown in Section 4.3.1. Comparing the results found for the candy cane and the aorta (Figure 5.14), we see that the axial velocity has the same behavior.

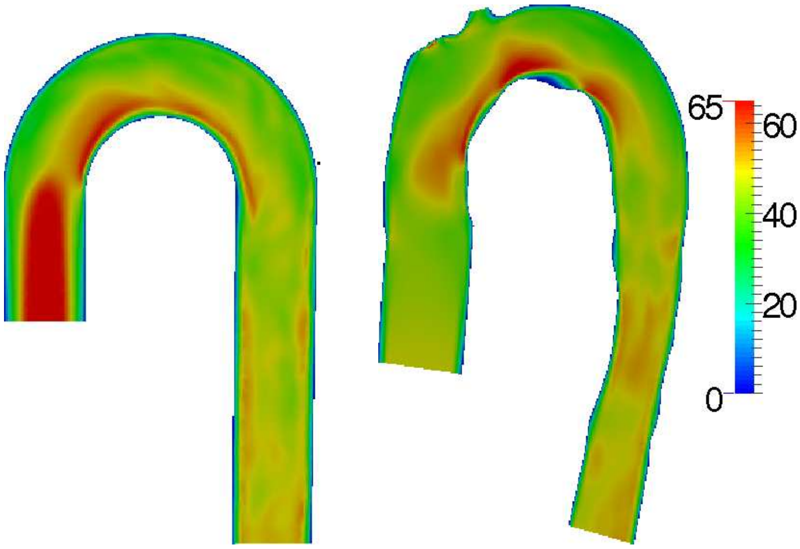

(a) Aorta (b) Candy cane

Figure 5.14: Comparison of the flow velocity [cm/s] between the aorta and the candy cane. From the figure we evince that the unsteady inflow is the main cause of the behavior of the axial velocity.

In the Figure [5.15], we show the axial velocity at six cross sections of the aortic arch at the systolic peak.

The maximum of the axial velocity at the entrance of the aorta, cross-section I, starts to move toward the inner aortic wall; furthermore it is shifted upward. In the cross-sections from II to V, the maximum of the axial velocity is total shifted to the inner wall of the primary curvature. But while in the sections II and III, the velocity shifted upwards, in sections IV and V it displaces downward. In the section VI, located in the descending aorta, the velocity becomes relatively uniformly in the sections. This results found are in agreement with the results of Farthing and Peronneau reported in the five chapter of the book [3].

The outcomes show that: **the flow is always displaced towards the inside of the curvature, when at the inlet is applied an unsteady flow**.

From our analysis we conclude that the behavior of the flow velocity dependents on the kind of inflow and on the morphology of the computational domain.

In particular in the case of the aorta results found in sections reflect the presence of multiple curvatures.

5.4.2 Velocity streamlines

The 3D flow visualization is based on 3D streamlines at three times: T_1, T_2, T_3. The streamlines are the lines whose tangent at each point is parallel to the velocity vector [18]. As is

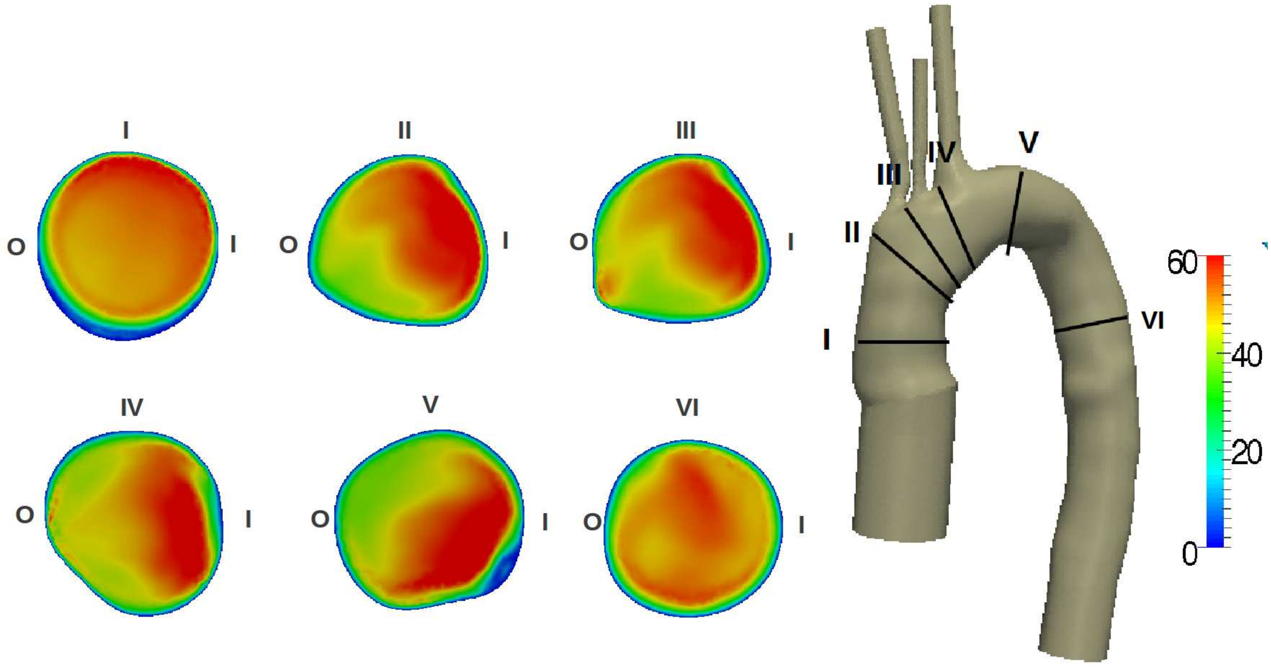

Figure 5.15: Qualitative analysis of the distribution of values of axial velocity in healthy aorta, shown for several cross-section at the peak of the inflow. The axial velocity is skewed toward the inner wall of the curves.

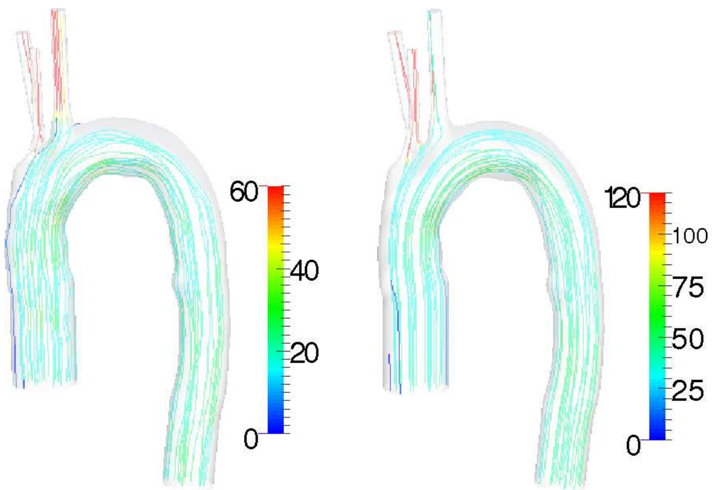

(a) T_1 (b) T_2 (c) T_3

Figure 5.16: Velocity streamlines for each investigated case on the median plane. The corresponding velocity magnitude [cm/s] is used to color each streamline.

evident from the Figure [5.23], flow patterns observed in this vessel along the primary curvature of the aortic arch, at the maximum acceleration and at the systolic peak, are linear, without vortex. This verifies that there are no morphological alterations that lead to disturbances in the flow. In the maximum deceleration, we start to see vortices along the inner wall of primary curvature.

5.4.3 Pressure

The Figure depicts the pressure distribution along the aorta at the systolic The Figure [5.24]

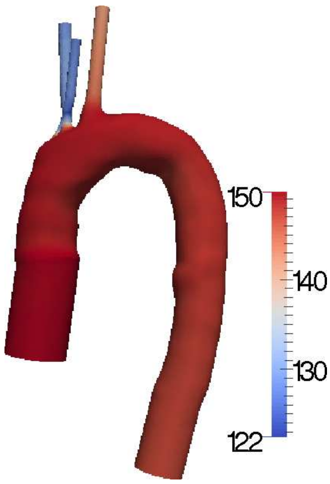

Figure 5.17: Contour plot representing the distribution of blood pressure [mmHg] along the aorta in the investigated case at the systolic peak.

shows that, the range of pressure at the systolic peak is about 120-150 [mmHg]. The maximum value of pressure at which a patient is considered healthy is about 120 [mmHg]. The values found through simulation do not differ much from the normal values. In addition we have to consider that in our case there are several possible sources of error:

- The inflow is not patient-specific;
- We assumed that the wall are rigid;
- Error introduced by the simulation, for example due to the discretization of the domain, etc.

For this reason, considering the results found for the streamlines, we can say that the patient has a healthy geometry.

5.4.4 Vorticity

In the Figure [5.18] we can observe that the maximum values of vorticity are located between the branches and in their outer wall. But because from this image we can not get information

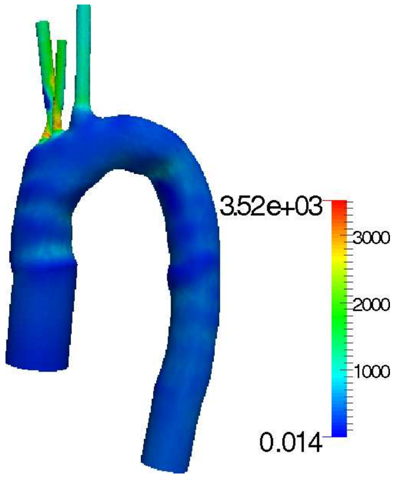

Figure 5.18: Plot representing the distribution of vorticity $[s^{-1}]$ along the aorta in the investigated cases at the systolic peak. the maximum values of vorticity are located between the branches and in their outer wall.

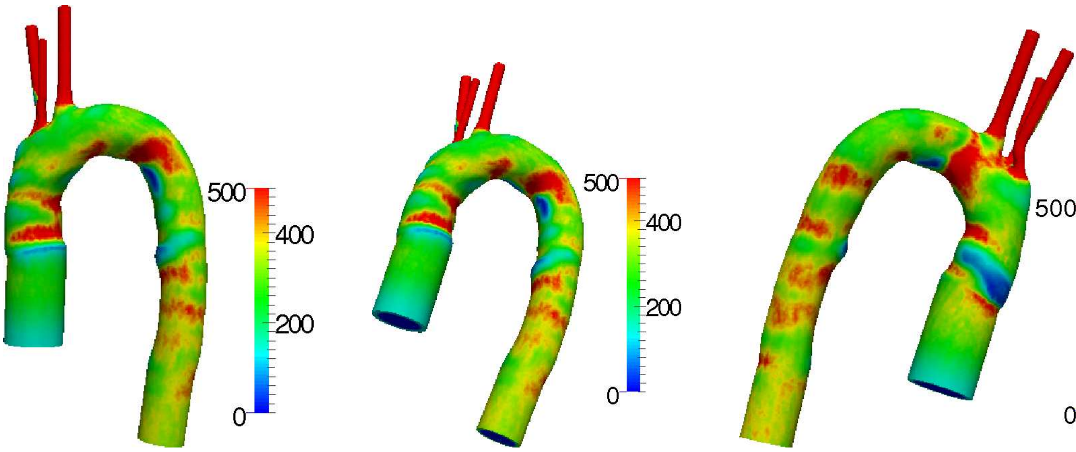

(a) Front (b) Below (c) Behind

Figure 5.19: Analysis of the vorticity $[s^{-1}]$ in the aortic arch from three points of view: frontal, from below and from behind. The figure shows that the vorticity is maximum at the inner wall of the curve

regarding the trend of vorticity in the aortic arch, we decided to rescale the range in which we assess it.

The Figure 5.19 shows us that the systolic peak systolic maximum values of vorticity are at the inner wall of the curve. These results agree with those found for the candy cane with unsteady inflow.

5.4.5 Wall shear stress

The values of wss agree both with the results found for the vorticity in Section [5.4.4] and with the trend of wss in the candy cane with inflow unsteady (Section[4.3.3])

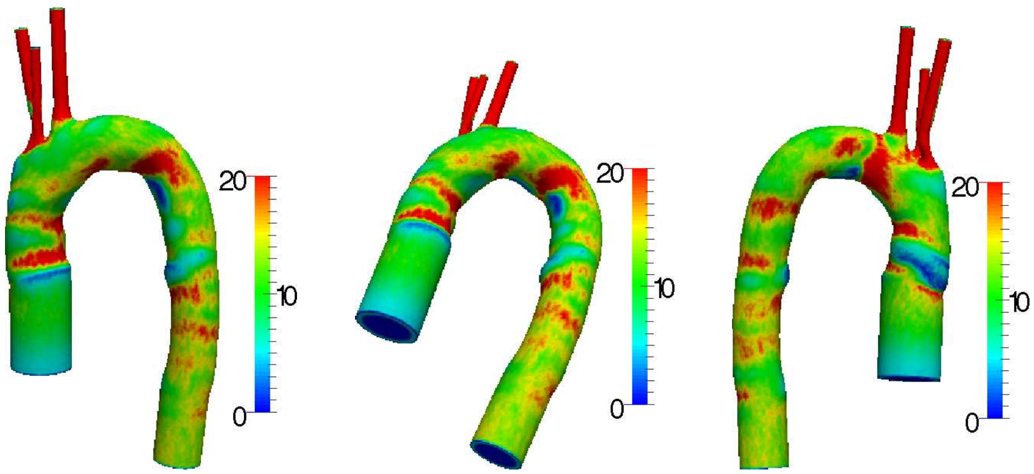

(a) Front (b) Below (c) Behind

Figure 5.20: Analysis of the wss $[dyne/cm^2]$ in the aortic arch from three points of view:frontal, from below and from behind; To simplify the analysis, we excluded the branches, focusing only the aortic arch. The figure shows that the vorticity is maximum at the inner wall of the curve

The Figure 5.26 shows us that at the systolic peak maximum values of wss are at the inner wall of the curve. These results agree with those found for the vorticity (Section 5.4.4) and with those found for the candy cane with unsteady inflow (Section 4.3.3).

5.5 Compare healthy case versus unhealthy

In this section we compare the hemodynamic of the clinical healthy case, previously studied, (case A) and the clinical case studied by Auricchio et all. in the article [1] (case B). The Figure depicts the vascular anatomy of the case B. As shows in the Figure [5.21] the pathological aortic arch shows a sharped angle that healthy case, leading to pronounced disturbance in the flow.

5.5.1 Axial flow velocity

In case A the maximum flow velocity is displaced gradually towards the inside of the curvature. In case B the first portion of the arch of the aorta is almost straight, here the velocity seems uniform in cross section; as the sharp angle starts, the maximum instantly moves toward the inner of the angle, and then returns uniform into descending aorta.

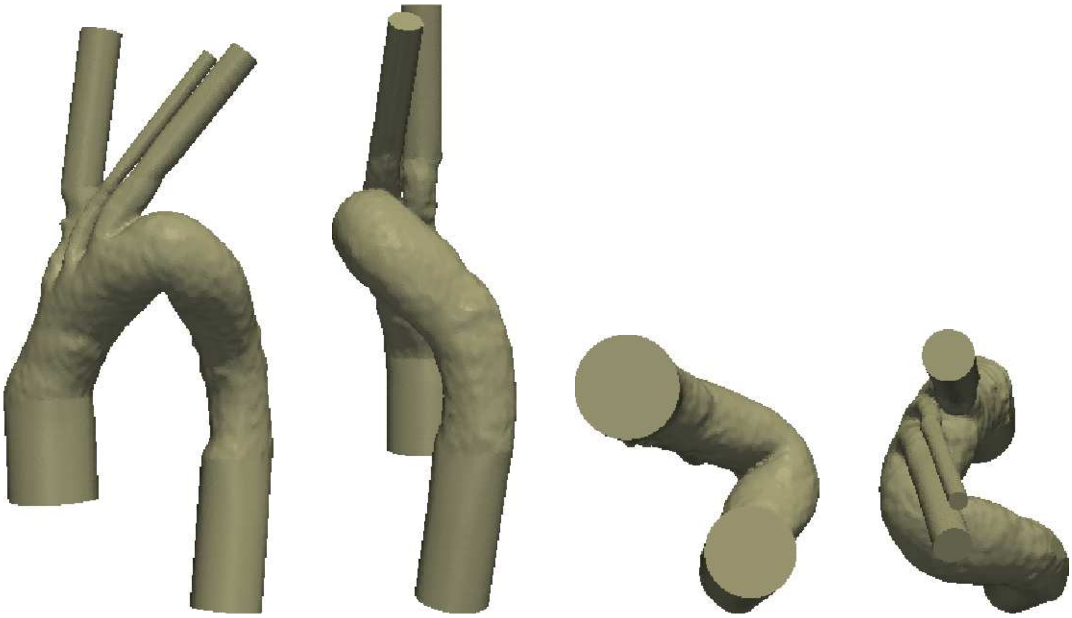

(a) Front view (b) Front from behind (c) View from above (d) View from below

Figure 5.21: Computational domains for the case B.

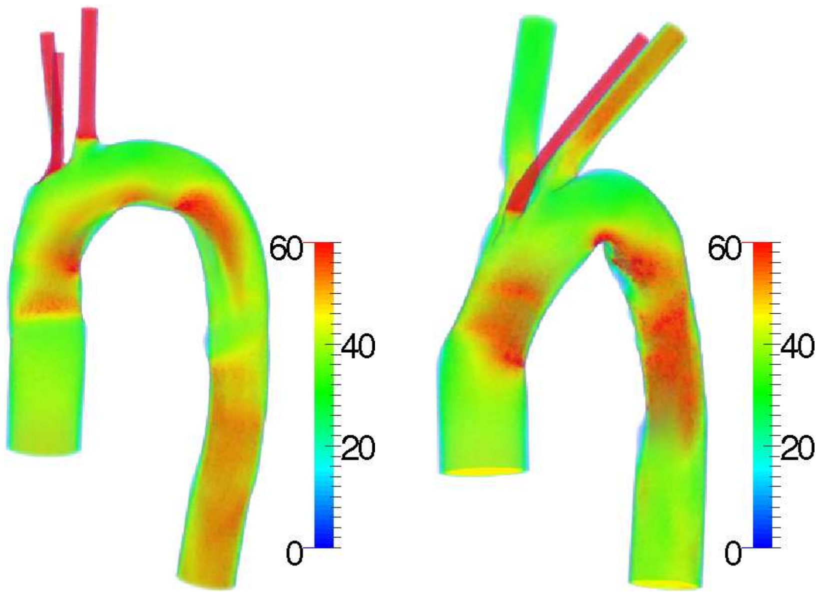

(a) Case A (b) Case B

Figure 5.22: In case A the axial velocity $[cm/s]$ moves gradually towards the inside of the curvature. In case B in the first portion of the aortic arch the velocity $[cm/s]$ is uniform in cross-section; at the sharp angle it moves toward the inner of the angle, and then returns uniform into descending aorta.

5.5.2 Streamlines

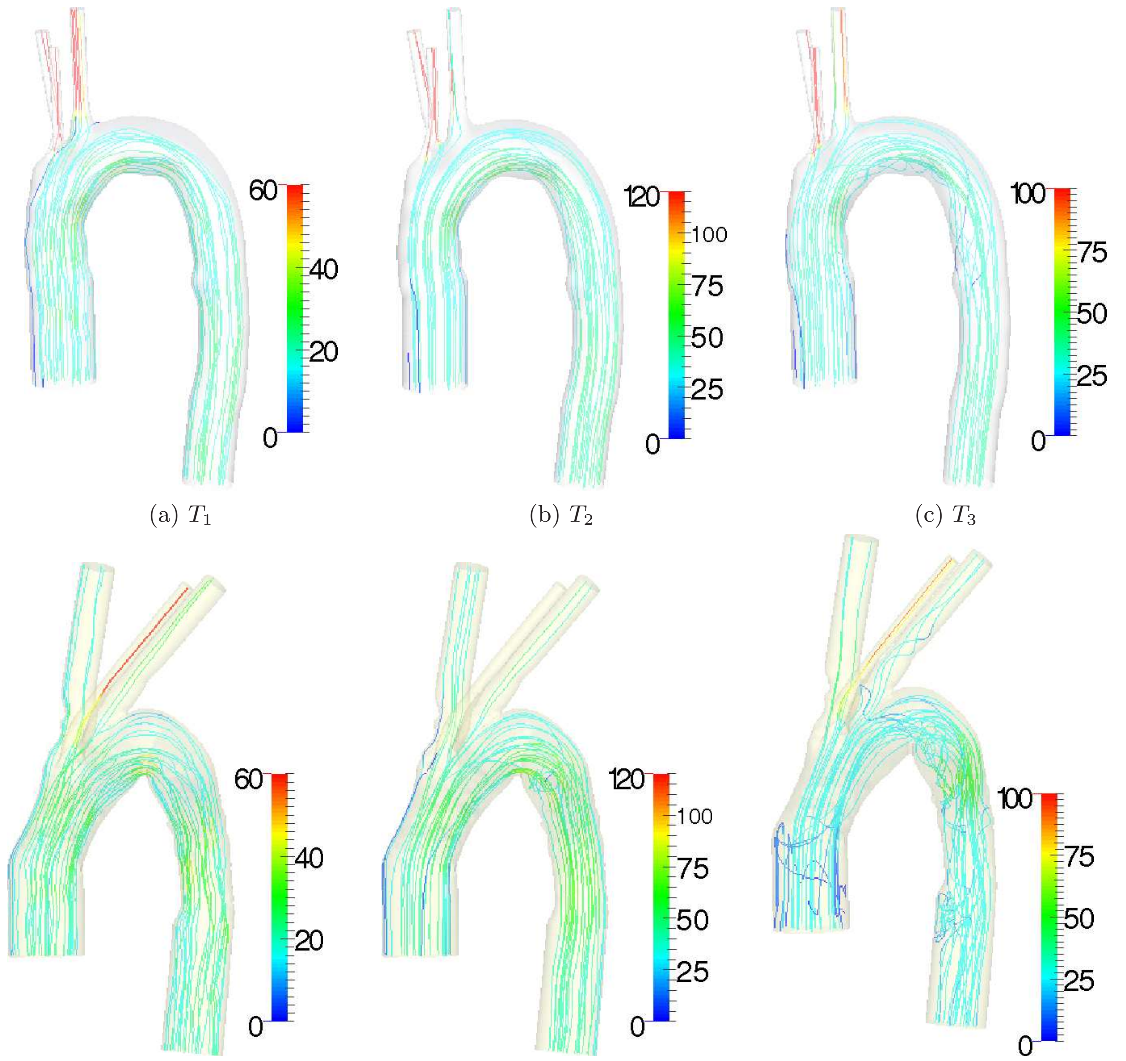

(a) T_1 (b) T_2 (c) T_3

(d) T_1 (e) T_2 (f) T_3

Figure 5.23: Velocity streamlines for each investigated case. The corresponding velocity magnitude [cm/s] is used to color each streamline.

As mentioned in Section 5.4.2, the streamlines of the case A does not have noise and represent the trend of the flow for a healthy geometry of the aortic arch.

The streamline path for the case B highlights the effects of the geometry distortion respect with healthy case. At time T1 the streamlines are linear. But to increase of the flow velocity, until its maximum in T2, because of malformation, the flow begins disturbed downstream the curvature. In particular we observe the flow separation; that becomes more visible for T3.

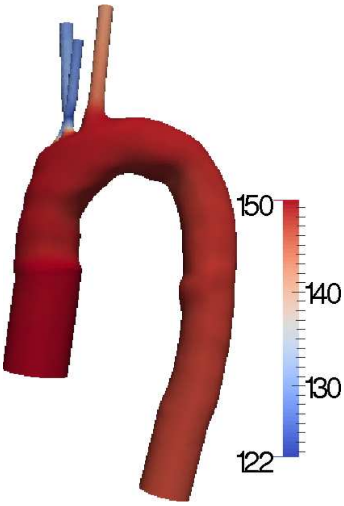

(a) Case A

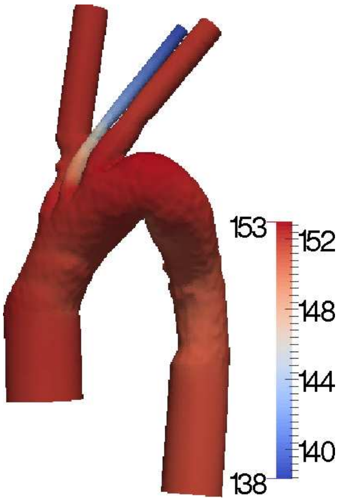

(b) Case B

Figure 5.24: Contour plot representing the distribution of blood pressure [mmHg] along the aorta in the investigated cases at the systolic peak.

5.5.3 Pressure

The pressure values in the two cases are comparable. Then, the strange shape of the case B does not involve variations of aortic pressure respect with healthy case. I conclude by saying that in this case (it is not available for all cases) the pressure does not give us information on the health status of the patient.

5.5.4 Vorticity

The case A is characterized by high values of vorticity in the inner wall of the curvature and small one in the outer. While in case B, the vorticity are more concentrated in the deformed bend and downstream of it, where there is the separation of the flows. The results in case B are due to the distortion of the aortic arch, it makes small the radius of curvature, so the number of Dean (see Section 4.1.1) increases and consequently the vorticity, as we have shown in Section **??** in Figure 4.15. We found that the patters of vorticity are directly related to the geometry of the computational domain.

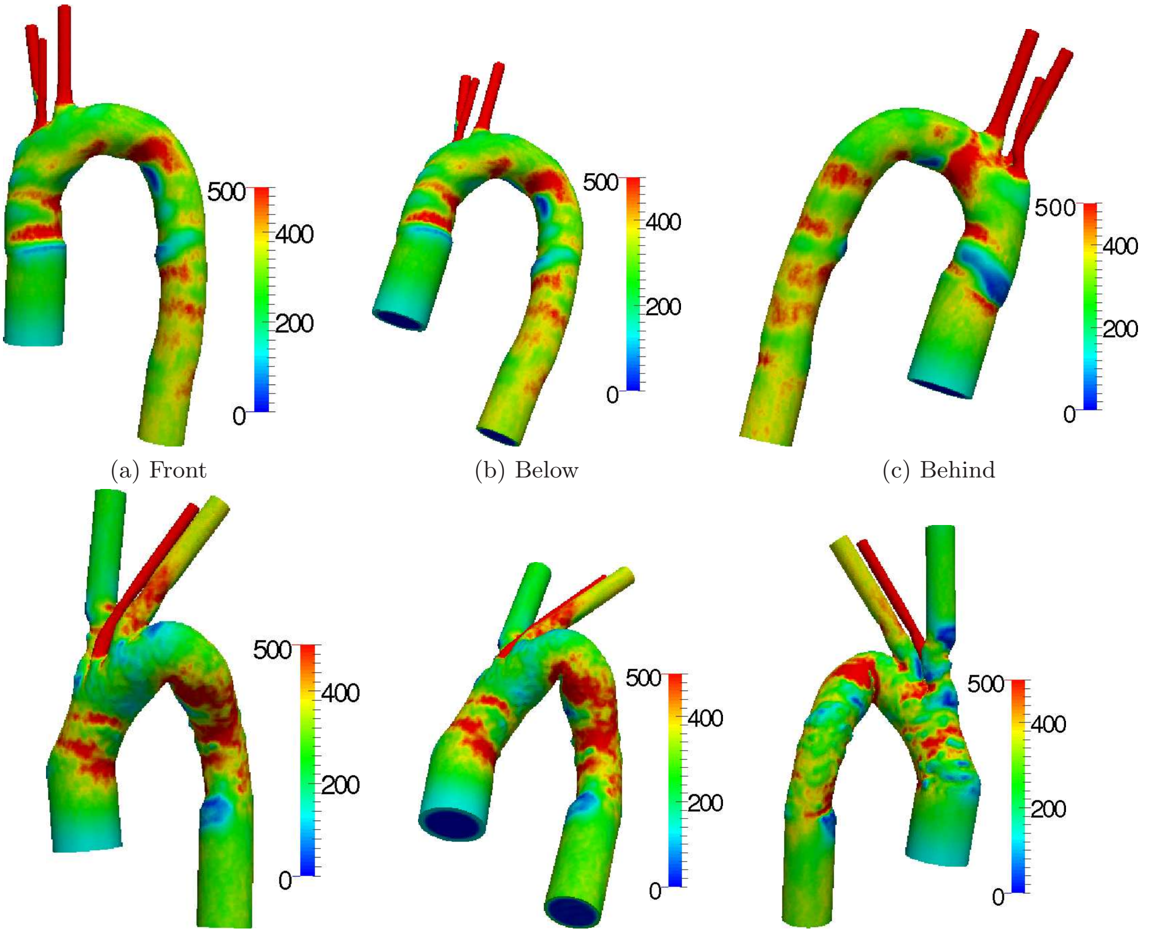

(a) Front (b) Below (c) Behind

(d) Front (e) Below (f) Behind

Figure 5.25: Analysis of the vorticity $[s^{-1}]$ in the aortic arch from three points of view:frontal, from below and from behind; To simplify the analysis, we excluded the branches, focusing only the aortic arch. The figure shows that the vorticity in the case A are high in the inner of curvature, while in the case B due to the sharp angle, the wss are high in the angle and downstream of it.

5.5.5 Wall shear stress

Here we compare the values of the wall shear stress (wss) at the systolic peak. The case A is characterized by high values in the inner wall of the curvature and small one in the outer. While in case B, the wss are more concentrated in the area most deformed and downstream of it, where there is the separation of the flows.

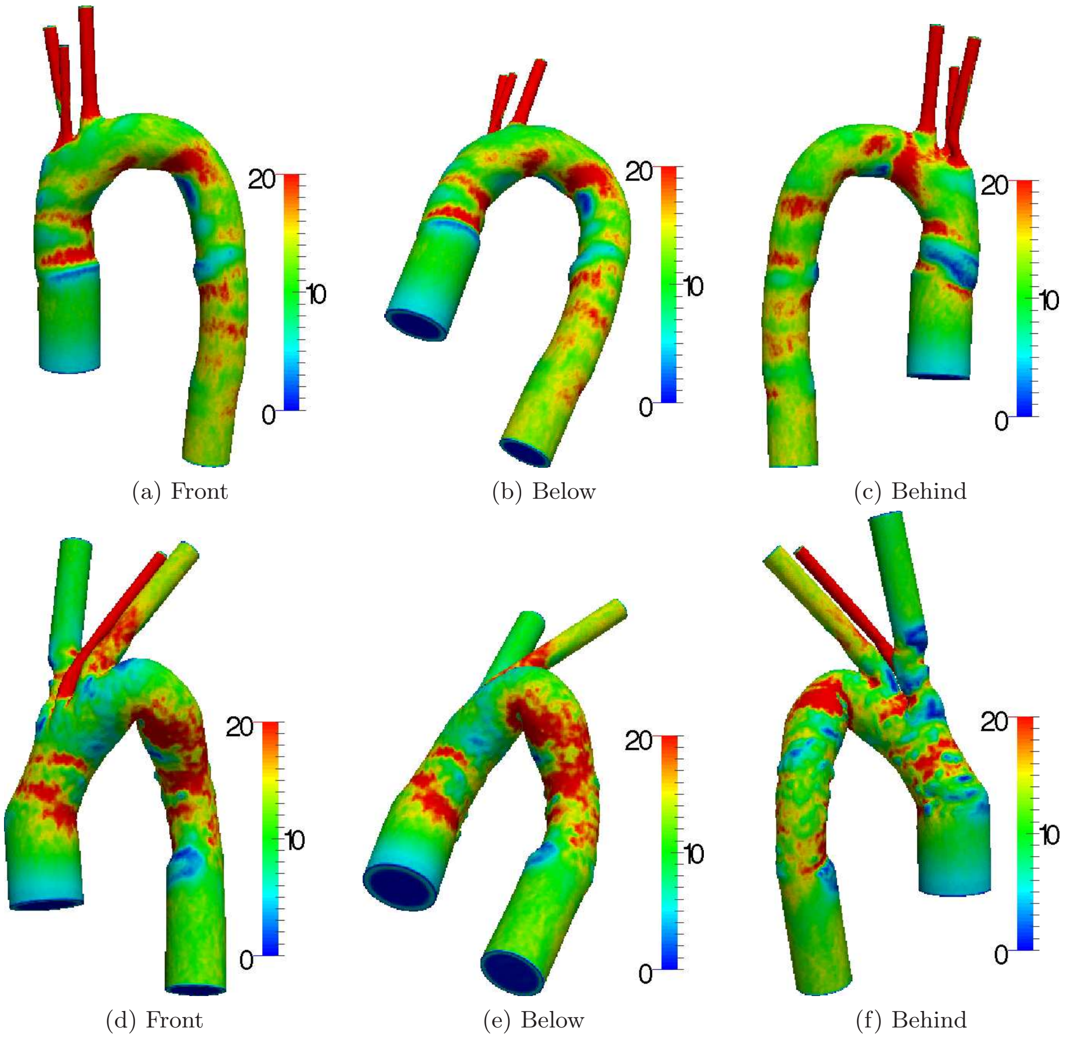

Figure 5.26: Analysis of the wss $[dyne/cm^2]$ in the aortic arch from three points of view:frontal, from below and from behind. To simplify the analysis, we excluded the branches, focusing only the aortic arch. The figure shows that the wss have the same patterns of vorticity.

Chapter 6

Conclusions

The aim of this thesis was to investigate the hemodynamics of a healthy aorta. To achive it, we performed computational fluid dynamics (CFD) analysis on the patient-specific vascular model derived from medical images. This allowed us to simulate the evolution of the blood flow in patient-specific geometry, approximating its real behavior.

In order to measure and interpret the flow dynamics in the complex geometry of the human aortic arch, it is important to understand the effect of curvature on the flow development.

To achieve this, we realized a simplified model of the aorta, which we called candy cane (its shape reminiscent sticks of sugar), with uniform entry flow. This analysis shows that as the flow moves around the curved tube, an imbalance between the centrifugal force and the radial pressure gradient generates secondary flows, i.e two vortices in the section perpendicular to the primary flow; The flow moves toward the outer wall, along the diameter, and returns towards the inner wall. The secondary flows also make that the maximum axial velocity is shifted toward the outside of the curvature.

The results found on the candy cane allows us to analyze in a simple and accurate manner the secondary flows and the trend of the axial velocity. However, in the real case we must consider that the blood flow is periodic pulsatile. Before moving to the study of real case we presented analysis of periodic pulsatile flow in a candy cane, that size is close to the human aorta one. The results showed an opposite behavior compared to the case where we apply a steady inflow. The maximum axial velocity moves toward the inner of curve tube and values of vorticity and wss are maximum in the inner wall.

Even though the studies described above on the flow development in curved tubes provide excellent insight on the nature of the secondary, the resulting skewing of the axial velocity profiles, the vorticity and wss; the blood flow in the human aorta is further complicated by the non circular cross-sectional geometry, secondary and tertiary curvatures, tapering, distensibility of the wall, and branch vessels emanating from the mid-arch region.

The results of the CFD analysis in this case, show that the flow is always displaced towards the inside of the curvature, it depends on the morphology of the computational domain, and on the unsteady flow applied a the inlet.

Another important result is the performance of wss. We proved that at the systolic peak maximum values of wss are found at the inner wall of the curve.

It should be noted that in this study several simplifications were made such as: blood continuum, rigid wall, boundary conditions and inflow no patient-specific.

Future works

Because the dystensibility of te aorta was not taken into account in our studies. The next step will be assess the hemodynamics of a healthy aorta taking into account its compliance, and calculate the error that we do by assuming the rigid wall.

Another relevant aspect to be further investigated is a noise-index, i.e an index that allows us to compare two cases to say quantitatively, if in a case the flow is more of another disturbed than another.

In the end, the greatest challenge will be development of boundary conditions patient-specific and application of a patient-specific inflow.

Appendix A

Starting Simulation

Starting lifev simulation is a task with several step; but before analyzing every single step it is important to learn how to access into the server.

- Open the terminal.
- Load the mesh file, earlier realized, to the server. We can do it typing in the terminal the following line:

  scp name_local_file client@IP_server

  This command put our file in the home of the server. If we want put it into a specific directory, we have to go into the server and create a new directory with the command:

  mkdir name_new_folder.

- Return in the local folder where there are our file mesh and type: scp name_local_file client@xxx.xxx.xx.xx:name_new_folder.
- Connect to the server typing:

  ssh client@xxx.xxx.xx.xx

  Input the password and press enter.

- In the same folder of the mesh file we must to put the files:
  - Inflow file
  - Data file
  - Bloodflow

- solveroptions.xlm To put this file that we need for the simulation, I suggest to upload it to the server home and then copy them whenever we need it, with the commands cp:

  scp file_name ../name_folder/

- Open data with a text reader and set suitable parameter values:

  initial time= -preload

  time step= period/1000 (because we discretize the time in 1000 interval)

  end time= number of cardiac cycle for example 3

  profil shape= parabolic or flat

  The labels for the boundary conditions have to be the same of this setting in the mesh file. in the section inflow we have to put in input_file, the name of our inflow file in the section fluid/space_discretization we set

  mesh_dir= ./ or the place of the mesh file (./ means that the mesh file is into the folder where we are.

  mesh_type= extension of the mesh file, for example .vol,mesh etc

  mesh_file = mesh file to simulate

  in the section exporter we can set to save the output of the simulation in a new folder, for do it we have to esc to the data file and create a new folder like:

  mkdir Results

  return in data file and set:

  post_dir= ./Results/ close the file data with pressing C-x C-c

  We have to do the export

  export PATH=/opt/lifev-env/openmpi/openmpi-1.6.4-install/bin:$PATH

  We start the simulation by typing:

  nohup mpirun -np number_core ./name_execute.exe > log &

  This instructions creates a file log within the simulation features. Now, if is all correct we can visualize how simulation progresses typing top. To write press q. Important : after we launched a simulation, if the computer has not finished yet and we want to get out of the server, we have to write exit, in this way the simulation continue, otherwise if we close the terminal without write it the simulation is broken.

  To block the simulation we have to use the command:

  killal name_of_application

Appendix B

Recover Data

In this case we want recover the data of our simulation,that are stocked in the folder called Results. In this case too, there are several steps like the previously case. We create a new folder; like name_original_folder_reduced. in this way:

mkdir name_original_folder_reduced

We copy the file data and Core_ensightImport.exe in the new folder. Data in this case is not the same of data used during the simulation.

We put in the folder that contains the new data file, we open it and after we modify it the way show below

mesh_dir= directory of the mesh file, for example /home/silvia/simulation_test

Parameters

Initial time= period * number of the second last cardiac cycle

end time= period *number of the last cardia cycle

time step= period00

numImport Proc=number of core

In the section exporter we set:

post_dir = path where we save the results of simulation

start = 201(in this ca we choose to analyze form 3° cardiac cycle, so the first snapshot of the last cardiac cycle start at 201)

save = 1 (this means that you have one snapshot every time step. So in the end, over the whole simulation we save 300 snapshots, equivalently to have the following time step: period*10

multimesh = false

time_id_width = 3

exportMode = 1

floatPrecision = 1

numImportProc = 1

We have to do the export:

export LD_LIBRARY_PATH=
/opt/lifev-env/openmpi/openmpi-1.6.4-install/lib:$LD_LIBRARY_PATH

Now we have to launch the command:

nohup ./Core_ensightImport.exe >log &

Now we go out to the folder we were and compress it:

tar -cvjf name_folder_with_redults_of_simulation.tar.bz2
name_folder_with_redults_of_simulation

Send the file create in the previously step from the server to our pc:

scp name_file client@your_ip: /path_of_we_want_download_the_file/

or esc from the server nd type in tne terminal:

scp client@server_ip:path_of_our_compress_file/
/path_of_we_want_download_the_file/

If we are still in the serve, have to go out and unzip the file.tar.bz2

tar xvfi name_folder_with_redults_of_simulation.tar.bz2

Bibliography

[1] Auricchio, F., M. Conti, A. Lefieux, S. Morganti, A. Reali, F. Sardanella, F. Secchi, S. Trimarchi, and A. Veneziani (2013). Patient-specific analysis of post-operative aortic hemodynamics: a focus on thoracic endovascular repair (TEVAR). *Computational Mechanics*.

[2] Buchanan, J. R., C.Kleinstreurer, S. Hyun, and G. Truskey (2003). Hemodynamics simulation and identification of suscetible sites of atheroclerotic lesion formation in a model abdomnal aorta. *Journal of biomechanics 36*, 1185–1196.

[3] Chandram, K. (2001). *Biomechanical Systems: Techniques and Applications, Volume II*. CRC Press,.

[4] Chandran, K. B., W. M. Swanson, D. N. Ghista, and H. W. Vayo (1979). Analysis of fully developed unsteady viscous flow in a curved elastic tube model to provide fluid mechanical data for some circulatory path-physiological situations and assist devices. *ASME J. Biomech. Eng. 101*, 114–123.

[5] Dean, W. R. (1928). The streamline motion of fluid in a curved pipe. *Phil. Mag. 5*, 73–695.

[6] Eustice, J. (1910). Flow of water in curved pipes. *Proceedings of the Royal Society of London. Series A, Containing Papers of a Mathematical and Physical Character 84*, 107–118.

[7] F.N. Van de Vosse, A.A Van Steenhoven, A. S. and J. Janssen. Steady lamiar entrance flow in a curved circular pipe.

[8] Formaggia, L., A. Quarteroni, and A. Veneziani (2009). *Cardiovascular mathematics Modeling and simulation of the circulatory system.*

[9] Kim, H. J., I. E. Vignon-Clementel, C. Figueroa, J. F. Ladisa, K. E. Jasen, J. A. Feinstein, and C. A. Taylor (2009). On coupling a lumped parameter heart model and

a three-dimensional finite element aorta model. *Annals of Biomedical Engineering 37*, 2153–2169.

[10] Kun, D. (1997). Blood flow in arteries. *Annual review fluid mechanics 29*, 399–434.

[11] Lyne, W. H. (1971). Unsteady viscous flow in a curved pipe. *Journal of Fluid Mechanics 45*, 13–31.

[12] M.A, Petrakis, G. Krahalios, and S. Kaplanis (2009). Steady flow in a curved pipe with circular cross-section. comparison of numerical and experimental results. *The open fuels & energy science journal 2*, 20–26.

[13] Munson, Young, and Okiishi (2005). *Fundamentals of fluid Mechanics.* 5th.

[14] Ronald, D. and L. Panton (1984). *Incompressible Flow.* Wiler.

[15] Shahcheraghi, N., H.A.Dwyer, A. Cheer, A. Barakat, and T. Rutaganira (2002). Unsteady and three-dimensional simulation of blood flow in the human aortic arch. *Journal of Biomechanical Engineering 124*, 378–387.

[16] Smith, F. (1976). Flow into a curved pipe. *Proceedings of the Royal society of London. Series A. Mathematical and physical sciences 351*, 71–87.

[17] Taylor, C. and C. Figueroa (2009). Patient-specific modeling of cardiovascula maechanics. *the annual review of Biomeical engineering*, 109–126.

[18] Temam, R. and A. Miranville (2005). *Mamathematical modeling in continuum mechanics.*

[19] W. R.Dean, J. M. H. (1927). Note on the motion of fluid in a curved pipe. *Phil. Mag. 20*, 208–223.

[20] Yoshizumi, M., J.Abe, K. Tsuchiya, B. Erk, and T. Tamaki (2003). Stress and vascular responses:atheroprotective effect of laminar fluid shear stress in endhotelial cell:possible role of mitogen-activated proteinkinases. *Journal of pharmacological sciences 91*, 172–176.